Ultrahigh flux of direct laser-accelerated electrons, MeV photons, and neutrons from overdense polymer foams

Parysatis Tavana*
Institute of Optics and Quantum Electronics (IOQ), Friedrich Schiller University Jena, Jena, Germany and Institute for Applied Physics (IAP), Goethe University Frankfurt, Frankfurt am Main, Germany

Mikhail Gyrdymov
Institute for Applied Physics (IAP), Goethe University Frankfurt, Frankfurt am Main, Germany

Jakub Cikhardt and Jan Novotny
Faculty of Electrical Engineering, Czech Technical University in Prague, Prague, Czech Republic

René Kalla
Institute for Applied Physics, Technical University of Darmstadt, Darmstadt, Germany

Pascal Boller
Institute for Applied Physics, Technical University of Darmstadt, Darmstadt, Germany
GSI Helmholtzzentrum für Schwerionenforschung, Darmstadt, Germany and Helmholtz Forschungsakademie Hessen für FAIR, Darmstadt, Germany

Thomas Kühl, Jan Glorius, Uwe Spillmann, Alessandro Tentori, and Ekaterina Kozlova
GSI Helmholtzzentrum für Schwerionenforschung, Darmstadt, Germany

Nikolai Bukharskii
Lebedev Physical Institute RAS, Moscow, Russia and National Research Nuclear University MEPhI, Moscow, Russia

Christian Spielmann
Institute of Optics and Quantum Electronics (IOQ), Friedrich Schiller University Jena, Jena, Germany

Olga N. Rosmej
Institute for Applied Physics (IAP), Goethe University Frankfurt, Frankfurt am Main, Germany
Helmholtz Forschungsakademie Hessen für FAIR, Darmstadt, Germany and GSI Helmholtzzentrum für Schwerionenforschung, Darmstadt, Germany

(Received 26 June 2025; revised 15 December 2025; accepted 12 January 2026; published 2 March 2026)

Ultrabright, well-collimated MeV bremsstrahlung radiation was generated through the interaction of high-current electron beams produced via direct laser acceleration (DLA) with a high-Z converter. The DLA mechanism was initiated by a 200 TW, subpicosecond PHELIX laser pulse at a moderately relativistic intensity of (1–2) $\times 10^{19}$ W cm^{-2}, delivering approximately 60 J of energy into preionized, overcritical-density foam targets. The electron spectrum measured along the laser axis exhibited an effective temperature of approximately 30 MeV and energies exceeding 100 MeV, with a total charge of about 300 nC for electrons with energies > 1.5 MeV (ponderomotive potential), while 100 nC of them is directed along the laser axis within a half-angle cone of 12°. The directed fraction of DLA electrons with energies exceeding 7.5 MeV carries a charge of 20 to 30 nC, corresponding to a flux up to 2×10^{24} sr^{-1} s^{-1}. These high-current relativistic electron beams efficiently generate MeV x-rays, enabling the subsequent production of isotopes, positrons, and neutrons with exceptional yield and application potential. In laser shots employing overcritical-density foam targets placed in front of a high-Z converter, bremsstrahlung photons with energies up to 70 MeV were generated and analyzed via nuclear activation of tantalum and gold. The formation

*Contact author: tavana@iap.uni-frankfurt.de

of the isotopes ^{174}Ta and ^{190}Au, whose photonuclear cross-section peaks at approximately 65 MeV, confirmed the presence of high-energy photons. In contrast, no activation was observed in control shots where the laser was directed onto the converter without foam, indicating that high-energy photon generation is intrinsically linked to the DLA process in the preionized foam targets. Autoradiographic measurements revealed a divergence of the bremsstrahlung beam of approximately 22° (half-angle) in the 14–21-MeV range. These diagnostics indicate an unprecedented photon flux of approximately 2×10^{22} sr^{-1} s^{-1}, corresponding to about 10^{11} photons per shot with energies exceeding 7.5 MeV. The conversion efficiency of focused laser energy to bremsstrahlung photons is greater than 1% (within the FWHM of x-ray beam and laser beam). More than 2×10^9 photoneutrons per shot were emitted isotropically, corresponding to a peak flux of 2×10^{20} cm^{-2} s^{-1} (4×10^{18} cm^{-2} s^{-1} J^{-1} of laser energy on target). This approach demonstrates a robust and scalable method for generating ultraintense MeV photon beams at kilojoule, petawatt-class laser facilities operating at moderate relativistic intensities, with strong implications for high-energy-density physics and nuclear astrophysics research.

DOI: 10.1103/5mpy-2jw5

I. INTRODUCTION

Laser-driven MeV x-rays have potential applications in a wide range of fields, including medicine (e.g., radiation therapy) [1] and biology [2], radiography of high-energy-density (HED) matter in experiments relevant to inertial confinement fusion (ICF) [3,4], laser-driven nuclear physics [5,6], and laboratory astrophysics [7,8].

The development of state-of-the-art lasers operating at ultrarelativistic intensities has enabled the generation of directed beams of MeV photons using all-optical inverse Compton scattering in the strongly nonlinear regime. In an experiment performed with a 4-PW laser at the Center for Relativistic Laser Science (CoReLS) in South Korea, the interaction of 3.5-GeV electrons with optical light resulted in a continuous spectrum containing up to 6×10^7 photons with energies above 10 MeV [9].

Nevertheless, bremsstrahlung produced by laser-accelerated relativistic electrons traversing high-Z materials remains one of the simplest and most effective methods for generating short, intense bursts of photons in the tens-of-MeV range, with high conversion efficiency even at moderately relativistic laser intensities [10,11]. Early experiments demonstrated that, rather than directly irradiating the converter with a relativistic-intensity laser pulse, it is significantly more efficient to first accelerate electrons via laser-plasma interaction and then direct the resulting electron beam onto a high-Z converter [12].

To this end, various mechanisms for laser-driven electron acceleration have been extensively investigated. One prominent mechanism is laser wakefield acceleration (LWFA), which operates optimally in tenuous, underdense plasmas and requires ultrashort laser pulses shorter than the plasma wave period. The so-called bubble or blowout regime of LWFA [13,14] enables the acceleration of electrons to GeV energies [15,16]. However, this comes at the cost of a low beam charge (typically 10–100 pC) and a limited overall laser-to-hot-electron conversion efficiency in subcritical plasmas.

The small flux achieved with LWFA is a limitation for applications that require moderate energies (10–100 MeV) and high fluxes. An example of such applications is the exploitation of photonuclear reactions in the region of the giant dipole resonance (GDR) [17]. For instance, photons in the tens-of-MeV range can induce neutron production via photonuclear reactions [18,19] or generate medical radioisotopes for positron emission tomography (PET) [2]. They can also be used to characterize the elemental composition of materials (from cultural heritage to geological samples) using the so-called photon activation analysis (PAA) method [20,21].

Enhancing the laser-to-MeV electron and MeV x-ray coupling efficiency remains a key objective of ongoing research at large-scale, high-energy, picosecond laser facilities. This is particularly important for the development of diagnostic tools in HED physics, where both high photon energy and high photon flux are essential. By increasing the electron plasma density up to 1%–10% of the critical density (with $n_c = 1 \times 10^{21}$ cm^{-3}) for a 1-μm laser wavelength and using longer laser pulse durations (i.e., longer than the plasma wave period), self-modulated laser wakefield acceleration (SM-LWFA) becomes the dominant acceleration mechanism. In this regime, a laser pulse of relativistic intensity ($>10^{18}$ W cm^{-2}) and picosecond duration propagates through an underdense plasma and generates plasma waves via resonance self-modulated instability (RSMI) [22,23] or Raman forward scattering (RFS) [24].

The SM-LWFA regime provides a platform for generating of broadband x-ray sources at large kJ- and sub-kJ-class picosecond laser facilities such as Titan and OMEGA EP in the USA [25–29], and currently at the Petawatt Aquitaine Laser (PETAL) of the Laser Mégajoule (LMJ) in France [30]. Experiments conducted at these facilities

report, on the one hand, high electron energy and charge, and on the other hand, process instabilities [31] and, in some cases, a strong deviation of the electron beam from the laser axis [27].

At facilities such as the Advanced Radiographic Capability (ARC) at the National Ignition Facility (NIF), where kJ-scale laser energy is focused into submillimeter focal spots, the use of a gas jet is not possible. Instead, a compound parabolic concentrator (CPC) is employed to geometrically focus the laser to a spot size of 25–50 μm [32]. Using a CPC in combination with a high-Z converter has been shown to significantly enhance the effective laser intensity and increase high-energy x-ray and positron production by up to an order of magnitude [3].

In the commissioning experiments at the PETAL facility, electron beams with an effective temperature of 8.3 MeV were produced at a laser intensity of 8×10^{18} W cm^{-2} in vacuum by placing a layer of CH (plastic) in front of an aluminum target. The plastic layer was preheated by a low-level nanosecond pedestal caused by amplified spontaneous emission (ASE), transforming it into a plasma with an exponentially decaying density profile [33], where effective electron acceleration occurred. This highlights the beneficial role of preformed plasma in improving laser-to-electron energy transfer, particularly in systems with large-f-number focusing optics.

Further increasing the target density to near-critical electron density (NCD) leads to the generation of beams of superponderomotive electrons carrying hundreds of nC of charge. Experiments with long-scale, low-density polymer foams [34] at the 200-TW PHELIX laser facility demonstrated this effect. In these experiments, foam layers converted into plasma by a controlled nanosecond pulse were irradiated by a subpicosecond pulse of moderate relativistic intensity. Measurements revealed a more than tenfold increase in the effective temperature and charge of superponderomotive electrons propagating along the laser axis compared with the irradiation of conventional foils [35,36]. This enhancement was attributed to direct laser acceleration (DLA) of electrons in long-scale NCD plasmas [37,38] and resulted in ultrabright betatron radiation [39,40], as well as efficient production of multi-MeV bremsstrahlung, photonuclear isotopes, and neutrons [19,36,41].

DLA-based electron sources, achieving up to 30% conversion efficiency of laser energy into electrons exceeding 2 MeV [36], are promising candidates for ultrabright MeV photon sources. These high-current, directed electron beams, when incident on a high-Z converter attached to the rear of the foam target, produce directed gamma radiation with an effective temperature of 10–15 MeV and photon energies exceeding 50 MeV [19,36,41,42]. This radiation has been verified through the detection of short-lived isotopes (e.g., ^{192}Au and ^{176}Ta) [19,36,41] and by high-yield neutron production [19].

In this work, we study the ultrahigh flux of MeV photons and neutrons obtained at moderate relativistic intensities [approximately (1–2) $\times$ 10^{19} W/cm^2] using 15 mg cm^{-3} polymer foams, which are overcritical for a 1 μm laser wavelength. The focus of this research was on employing high-current, well-directed beams of superponderomotive electrons generated in these foams for the efficient production of x-rays in the region of GDR. The resulting x-rays in the tens-of-MeV range can, in turn, effectively initiate photonuclear reactions and photoneutron production, which are of interest for applications in nuclear physics and laboratory astrophysics.

This paper is structured as follows: Sec. II outlines the laser system, target configuration, and experimental diagnostics. Section III presents the experimental results, including the characterization of superponderomotive electrons in Sec. III A, as well as gamma spectroscopy and the generation of MeV x-rays and neutrons in Sec. III B. Section IV describes GEANT4-based Monte Carlo simulations modeling the production of bremsstrahlung photons, isotopes, positrons, and neutrons. Finally, Sec. V summarizes the key findings and presents the conclusions.

II. EXPERIMENTAL SETUP

The experiment was conducted at the Nd:glass Petawatt High Energy Laser for Heavy Ion Experiments (PHELIX) facility at the Helmholtz-Zentrum GSI in Darmstadt, Germany [43,44]. An s-polarized laser pulse with a fundamental wavelength (λ) of 1.053 μm, a duration (τ_{las}) of 750 $\pm$ 250 fs, and an energy of 75 $\pm$ 5 J (measured before the compressor) was used. Approximately 80% of this energy 60 $\pm$ 4 J was delivered to the target, with the remaining 20% lost in the compressor.

The pulse was focused onto the target using an off-axis parabolic mirror with a focal length of 150 cm (f/5). The resulting elliptical focal spot, measuring 15 and 12 μm (FWHM), contained an energy of 20 $\pm$ 2 J. This configuration yielded a peak laser intensity of approximately (1–2) $\times$ 10^{19} W cm^{-2}.

The targets consisted of polymer foams with a composition of 71% C, 27% O, and 2% H by mass (hereafter referred to as CHO). The foams had a density of 15 mg cm^{-3} and a thickness of 500 μm. They were supported with 1-μm-thick copper foils. High-Z converters consisting of two 1-mm-thick tantalum plates (6 $\times$ 6 mm^2) and one 1-mm-thick gold plate (7.5 $\times$ 7.5 mm^2) were attached to the rear side of the foam [see Fig. 1(a)].

In the case of fully ionized CHO plasma, the maximum plasma electron density for, e.g., 15-mg cm^{-3} CHO foam can reach 4.5n_c, where $n_c = 1 \times 10^{21}$ cm^{-3} is the critical electron density for a laser wavelength of $\lambda = 1$ μm. A submillimeter-thick NCD plasma was produced by sending a well-controlled nanosecond pulse onto the foam to initiate an ionization wave [45]. The impact of the

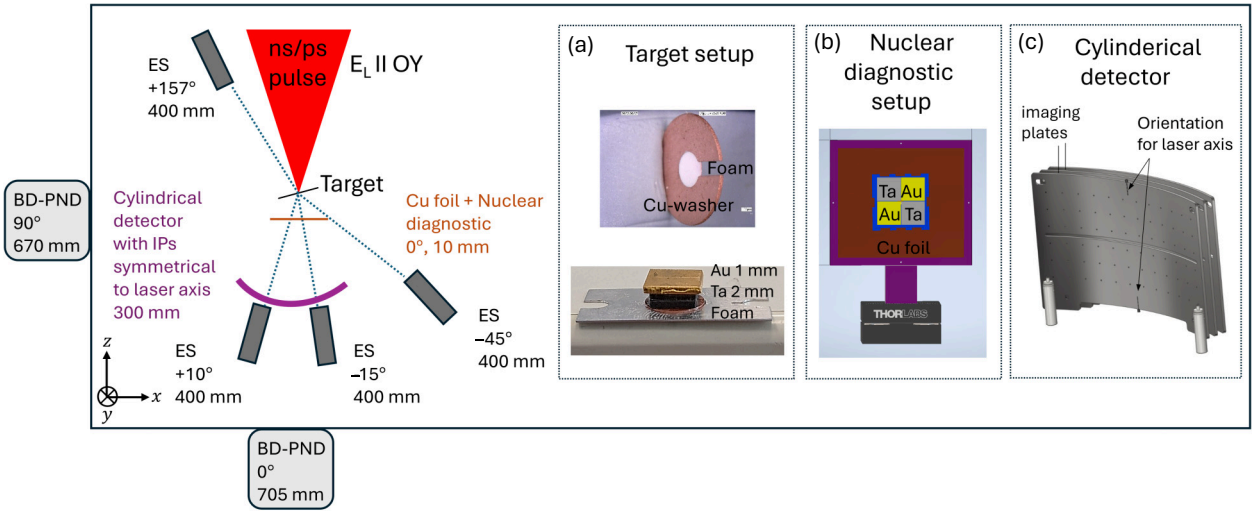

FIG. 1. Top view of the experimental setup. A nanosecond and a subpicosecond PHELIX laser pulse are focused onto a foam target embedded in a copper washer and coupled to a 3-mm-thick high-Z converter [inset (a)]. Electron diagnostics include four magnetic spectrometers placed at angles of $+10°$, $-15°$, $-45°$, and $+157°$ with respect to the laser axis, as well as a cylindrical detector for angular distribution measurements [inset (c)]. The gamma-ray distribution is measured via autoradiography of a copper foil. The MeV x-ray energy spectrum is obtained using a filter grid of gold and tantalum foils positioned behind the copper foil [inset (b)].

nanosecond pulse on the resulting plasma profile and on the DLA process is thoroughly analyzed in our recent publication [46]. The nanosecond laser pulse was optimized for the foam targets; it had an energy equal to 3% of the main pulse energy, a duration of 3 ns, and arrived 5 ns before the picosecond pulse reached the target.

A comprehensive characterization of the primary radiation source—namely, DLA electrons—requires knowledge of the energy and angular distributions, as well as the charge per pulse and directional stability of the emission. To this end, the experimental setup (shown in Fig. 1) incorporates four magnetic electron spectrometers with a field strength of 0.99 T, each equipped with a bio-imaging analyzer system, image plate multipurpose standard (BAS-IP MS), as a detector. The energy resolution of the spectrometers, with entrance slits of 300 μm (width) and 1000 μm (height), was numerically simulated using two-dimensional (2D) B-field distributions measured inside the steel housing of the spectrometer. An experimental error in the energy measurements was found to arise mainly from the entrance slit and did not exceed 2%. This allowed reliable measurement of electron energies from 1.5 to 100 MeV. The spectrometers were positioned 400 mm from the target at angles of $+10°$, $-15°$, $-45°$, and $+157°$ relative to the laser axis to measure the local electron energy distributions. Their entrance slits were shielded by four 5-mm-thick Cu–W plates to reduce the background on the IP.

To characterize the angular distribution and pointing stability of the electron beam, two large-area BAS-IP MS plates were installed between three layers of 3-mm-thick stainless steel, shaped into semicylindrical segments with a curvature radius of 300 mm [see Fig. 1(c)]. A horizontal 4-mm-wide slit running along the midplane of the shielding allowed electrons to pass through and reach the magnetic spectrometers positioned behind this detector. The first image plate (IP), located behind the first shielding layer, recorded electrons with energies exceeding 3 MeV, while the second IP, located behind the second layer, was sensitive to electrons with energies above 7.5 MeV. The cylindrical stack was placed 340 mm from the interaction point and covered an angular range of 37° in the horizontal direction and 20° in the vertical direction. The correspondence between the IP signal generated by the electrons and the absolute number of electrons with energies >1.5 MeV was taken from Ref. [47]. For this purpose, the irradiated IPs were scanned using the same FLA700 scanner model and the same scanning parameters as in Ref. [47]. A detailed description of the magnetic spectrometers and the cylindrical diagnostic can be found in Ref. [36].

In addition, nuclear activation diagnostics were implemented to provide insight into the energy and angular distribution of the emitted MeV bremsstrahlung photons with $E > 7.5$ MeV. For this purpose, large-area copper foil (40×40 mm^2, 100 μm thick) was placed 10 mm behind the target to determine the angular distribution of MeV x-rays via autoradiography [48–50]. Directly behind the copper foil, a stack of activation materials consisting of two gold and two tantalum samples (each 7.5×7.5 mm^2, 1 mm thick) was used to provide information on the x-ray energy spectrum through subsequent gamma spectroscopy [see Fig. 1(b)].

After every shot, the activity of the samples was measured using two high-purity germanium (HPGe) detectors, with their signals processed by ORTEC 671 shaping amplifiers. The output of one amplifier was digitized through an ORTEC 928 multichannel buffer (MCB), while the other was connected to an ORTEC EASY-MCA multichannel analyzer system. To reduce the environmental background, the detectors were placed inside a 10–cm-thick lead housing.

Additionally, two bubble detectors—specifically personal neutron dosimeters [51]—each with a sensitivity of 14–16 bubbles per mrem, were mounted outside the PHELIX target chamber. One detector was positioned along the axial direction and the other along the radial direction with respect to the laser axis and the laser-matter interaction point. The distances from the interaction point to the detectors were 705 mm (axial) and 670 mm (radial). These devices are capable of detecting neutrons in the energy range 200–15 000 keV, which, in this experiment, were primarily produced via (γ, xn) reactions.

III. EXPERIMENTAL RESULTS

A. Production and measurement of DLA electrons

Our previous experiments on the interaction of relativistic laser pulses with preionized NCD foams have already demonstrated robust generation of high-current, relativistic electron beams exhibiting effective temperatures exceeding the ponderomotive potential by more than an order of magnitude [35,36,46].

In this work, we first characterize the energy spectrum, divergence, and charge of the electron beam produced in foams of initially overcritical density (500 µm thickness, 15 mg cm^{-3} density). According to 2D hydrodynamic simulations of ionizing wavefront propagation in structured foams, similar to those reported in [46] for NCD foams, the interaction of an ns pulse with overcritical foams resulted in the formation of a plasma layer of a few hundred micrometres with an electron density ranging from 10^{19} to 10^{21} cm^{-3}, followed by a sharp density rise near the foil. To avoid any distortion of the electron beam by high-Z material, the measurements were performed without a converter.

As shown in Fig. 2(a), the application of a nanosecond laser pulse to create an extended preplasma in aluminum (yellow data points) leads to a substantial increase in total charge, electron energy, and effective temperature—rising from 0.6 to 9 MeV—compared with a high-contrast shot on a 50-µm-thick aluminum foil (gray data points). This effect becomes even more pronounced when low-density foams preionized by a controlled nanosecond pulse are used, which can be attributed to the dominance of the DLA mechanism in near-critical-density plasma. In an exponentially decaying plasma density profile, the region where the density remains close to the critical value typically spans only 30–50 µm. The use of sub-millimeter-thick overcritical-density CHO foams, preionized by a nanosecond pulse, significantly extends the available acceleration length for DLA. Consequently, shots on preionized foams (500 µm thickness, 15-mg cm^{-3} density, supported by a 1-µm copper foil) show a pronounced increase in total charge and effective temperature, as indicated by the red, blue and green data points in Fig. 2(a). For example, the effective temperature of the electron fraction propagating at $-10°$ relative to the laser axis reached 26–29 MeV.

Figure 2(b) shows the measured spatial profile of the accelerated electrons (with energies above 7.5 MeV),

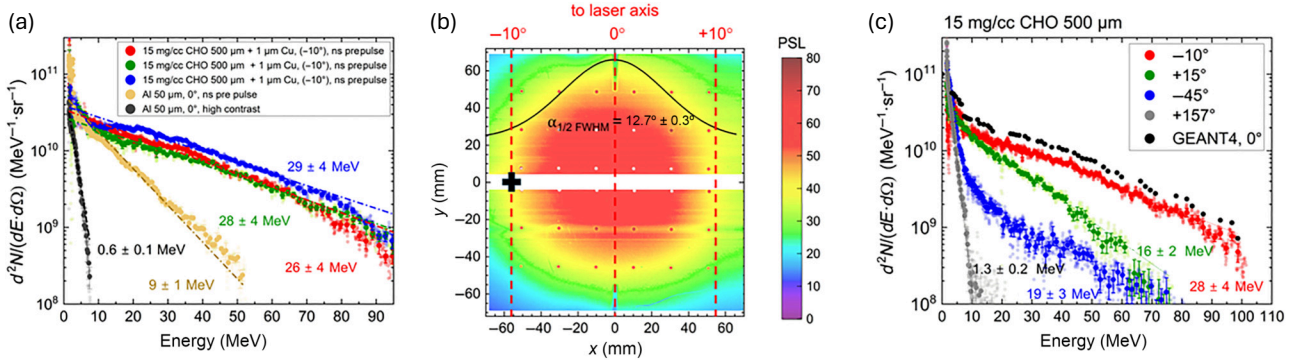

FIG. 2. (a) Electron spectra measured at 0° relative to the laser axis for a high-contrast shot on a 50-µm aluminum foil (gray) and for a shot with a preceding nanosecond prepulse on aluminum (yellow), showing an increase in both charge and effective temperature (up to 9 MeV) in the presence of the prepulse. Preionized CHO foams (red, green, blue), measured at $-10°$ relative to the laser axis, exhibit even higher effective temperatures of 26–29 MeV. (b) Angular distribution of electrons with energies > 7.5 MeV recorded on an image plate for a shot on preionized 500-µm CHO foam, indicating a well-collimated beam with a half-angle divergence of $\theta_{1/2} = 12.7° \pm 0.3°$. The cross at $-10°$ marks the position of the magnetic spectrometer. (c) Electron spectra from all four magnetic electron spectrometers for a shot on preionized 15–mg cm^{-3} CHO foam, showing a strongly forward-directed emission peaked along the laser axis.

recorded on the image plate of the cylindrical detector, indicating a half-angle divergence of $\theta_{1/2} = 12.7^\circ \pm 3^\circ$.

Figure 2(c) presents the angularly resolved spectra from all four magnetic spectrometers placed around the target for a shot on preionized 15–mg cm^{-3} CHO foam, further confirming that the electron emission is well peaked along the laser axis. Experimentally, the electron-beam charge was estimated from the spectral distribution of electrons, $d^2N/dE\,d\Omega$, measured at different angles relative to the laser axis and integrated over electron energies above the specified threshold. The electron beam was modeled with a Gaussian profile in the horizontal and vertical directions centered at the maximum of the IP image [Fig. 2(b)]. The accuracy of the beam charge estimation is 20% to 30%. Electrons above the 1.5-MeV ponderomotive threshold carry a total charge of 300 nC in 2π, with 100 nC directed into the 12.7° cone. For energies exceeding 7.5 MeV, relevant for bremsstrahlung in the GDR region, the charge reaches 80 nC in 2π, of which 20 to 30 nC falls within the same half-angle [Fig. 2(b)]. This corresponds to a flux of DLA electrons ($E > 7.5$ MeV) along the laser axis of approximately 2×10^{24} sr^{-1} s^{-1}, assuming that the electron bunch duration does not exceed that of the laser pulse.

To assess the reproducibility of the electron-beam parameters, six dedicated optimization shots were carried out under different ns-pulse conditions. Under optimal conditions—that is, a 5-ns prepulse delay with 3% of the main pulse energy—the effective electron temperature ranged from 26 to 29 MeV, with a mean of $27.7 \pm 1.5 -$ MeV. The total charge of electrons ($E > 7.5$ MeV) integrated over 2π, is 109 ± 25 nC, corresponding to a laser-to-electron conversion efficiency of $18\% \pm 3\%$.

The 5-ns delay with 3% prepulse energy was consequently adopted as the standard condition for generating MeV bremsstrahlung in subsequent shots. In these later experiments, low-density foams were combined with 3-mm-thick high-Z converters, where DLA-accelerated electrons deposited most of their energy. As a result, direct measurements of the primary electron properties were no longer feasible.

The combination of higher energy, increased charge, and improved beam collimation is essential for the efficient generation of ultrabright, directional MeV x-ray beams with photon energies falling within the GDR region.

B. Production and measurement of MeV x-rays in the GDR region and associated photoneutron emission

For the generation of x-rays in the tens-of-MeV range, the overdense foam layer was coupled with a millimeter-scale high-Z converter composed of two stacked 1-mm tantalum plates followed by a 1-mm gold plate. When DLA electrons, generated by a relativistic laser pulse in preionized overcritical-density foams, penetrate the converter material, a fraction of their energy is converted into bremsstrahlung radiation. The efficiency of this energy conversion increases with the charge and energy of the electron beam. Additionally, a higher atomic number of the converter material results in a greater fraction of electron energy being converted into photons.

A comprehensive review of electron-nucleus bremsstrahlung cross sections can be found in Ref. [52]. Monte Carlo simulations, such as those performed in GEANT4 [53], employ the bremsstrahlung cross-section tables developed by Seltzer and Berger [54].

The optimal converter thickness for efficient generation of MeV x-rays depends on the electron spectrum. As electrons propagate through the converter, they lose energy via both collisional and radiative processes, with bremsstrahlung becoming the dominant mechanism for electron energies above approximately 10 MeV. The optimal converter thickness for electron spectra generated from preionized 15-mg cm^{-3} CHO foams was investigated using GEANT4 simulations. The results indicate that a 3-mm-thick high-Z converter provides the most efficient production of x-rays with energies above 7 MeV (see Sec. IV for details).

To characterize the spectral and spatial distribution of the generated MeV bremsstrahlung, nuclear activation diagnostics were used. A set of activation plates—two gold and two tantalum samples—was arranged in a grid on the rear side of a large-area copper foil positioned behind the target [see Fig. 1(b)]. After each laser shot, the foils were analyzed using a low-background, high-purity germanium (HPGe) detector to identify radioactive isotopes produced via photonuclear reactions, based on their known γ-ray energies, emission intensities, and half-lives.

These reactions occur when high-energy bremsstrahlung photons excite the GDR of atomic nuclei, leading to neutron emission and the formation of radioactive isotopes. The resulting γ-ray decay spectra provide a quantitative measure of the photonuclear yields and thus serve as a diagnostic for the MeV x-ray spectrum generated in the interaction. The number of reactions (yield), denoted as Y, is determined by convolving the bremsstrahlung spectrum $\Phi(E_\gamma)$ with the energy-dependent cross section $\sigma(E_\gamma)$ of a photonuclear reaction:

$$Y = N_T \int_{S_n}^{\infty} \sigma(E_\gamma)\Phi(E_\gamma)\,\mathrm{d}E_\gamma, \tag{1}$$

where S_n is the threshold energy of the reaction and N_T is the number of target atoms irradiated. By combining the yields of different isotopes, it is possible to reconstruct the bremsstrahlung spectrum, as described in Ref. [55].

In this study, gold and tantalum plates were used as activation materials, consisting of 99.9% pure ^{197}Au and ^{181}Ta. Photonuclear activation in these materials probes the high-energy part of the bremsstrahlung spectrum above

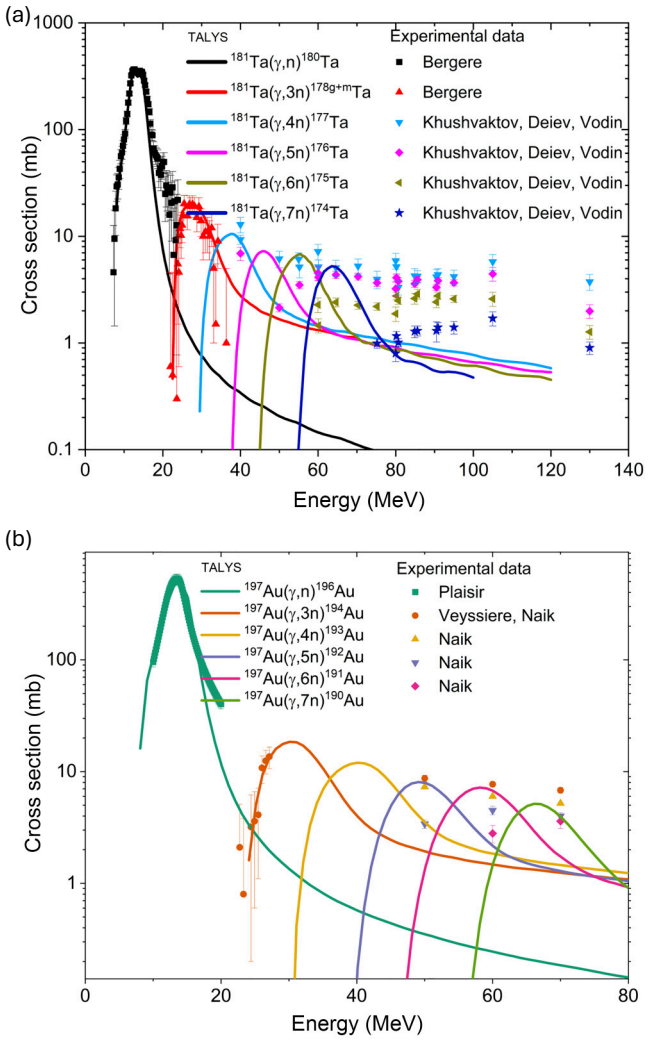

FIG. 3. (a) Cross sections for different ^{197}Au (γ, xn) reactions and (b) ^{181}Ta (γ, xn) reactions, simulated using the TALYS code and compared with experimental data from Ref. [57].

7.5 MeV, the threshold for the (γ, n) reactions in both nuclei.

The dependence of the cross sections of different (γ, xn) reactions (where x denotes the number of emitted neutrons, $1 \leq x \leq 7$) in ^{197}Au and ^{181}Ta on photon energy is shown in Fig. 3. The results obtained from simulations using the nuclear reaction code TALYS [56] are compared with experimental data retrieved from the EXFOR database [57]. Comprehensive nuclear reaction data for gold and tantalum (including reaction thresholds, half-lives of the resulting daughter nuclides, their decay modes, and the most intense gamma-ray lines) are provided in the Appendix A. After each shot, and following a chamber venting period of approximately 15–20 min, the activated nuclear probes were transferred to HPGe detectors for γ-ray spectroscopic analysis. These detectors were

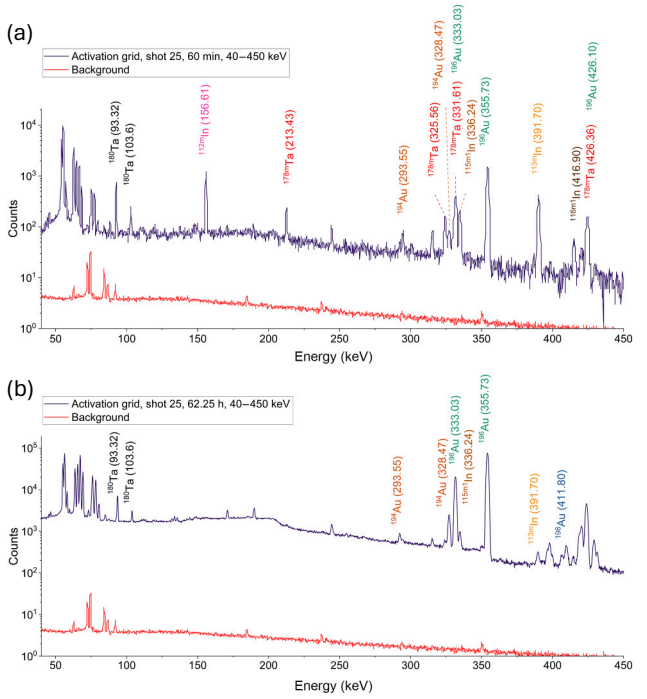

FIG. 4. Gamma-ray spectrum of the nuclear probes (Au, Ta, and In) in the energy range from 40 to 450 keV. (a) Spectrum recorded after a 1-h measurement; (b) spectrum recorded after a 62.25-h measurement.

precalibrated for both energy and efficiency using certified radioactive sources.

A representative γ-ray spectrum of the activation grid of a selected shot is shown in Fig. 4, covering the energy range from 40 keV to 450 keV. The upper panel corresponds to a 1-h measurement that began 23 min after irradiation, while the lower panel presents a spectrum from a 62.25-h measurement that began 5.12 h postirradiation. Prominent γ-ray lines are observed for several isotopes, including ^{196}Au, ^{194}Au, ^{192}Au, ^{180}Ta, and ^{178m}Ta. A separate discussion of indium-associated lines will be provided elsewhere, as these isotopes are produced through (γ, n), (n, γ), and (n, n') reactions in indium.

High activation yields were observed in a single laser shot, producing $(4.66 \pm 0.04) \times 10^7$ nuclei of ^{196}Au, $(5.35 \pm 0.29) \times 10^5$ nuclei of ^{194}Au, and $(1.25 \pm 0.04) \times 10^5$ nuclei of ^{192}Au in the activation probes; the corresponding (γ, n)cross-section peaks are at approximately 14, 30, and 50 MeV, respectively. In particular, only two of the four probes were made of gold. Assuming a comparable positioning and beam exposure for all probes [see Fig. 6(b)], the total yield of ^{196}Au isotopes is estimated to reach 10^8.

Preliminary results from the activation of gold targets via bremsstrahlung generated by an LWFA at ELI-NP, using a 1-PW laser system with peak intensities of $(2.0–2.5) \times 10^{20}$ W/cm^2, have yielded only $(4.1 \pm 0.4) \times$

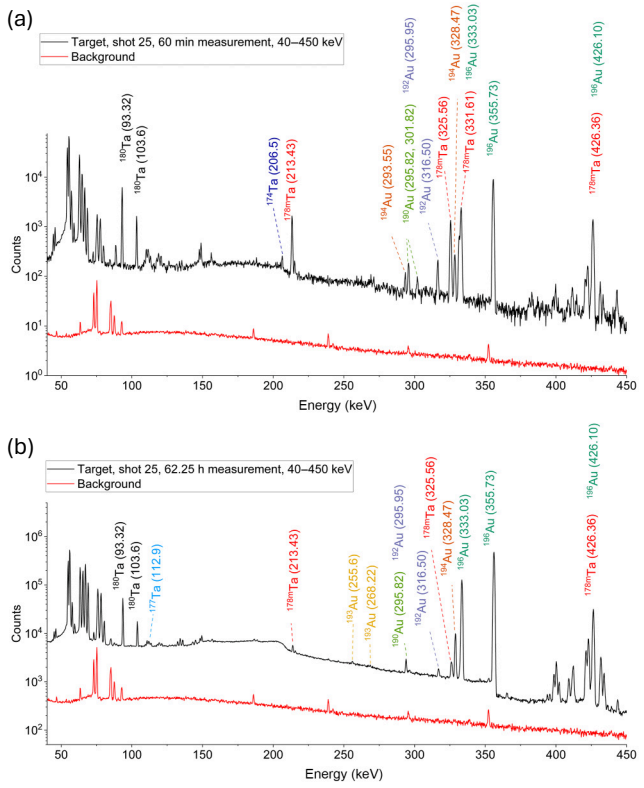

FIG. 5. Gamma-ray spectrum of the high-Z converter (2 mm Ta + 1 mm Au) in the energy range from 40 to 450 keV. (a) Spectrum recorded after a 1-h measurement; (b) spectrum recorded after a 62.25-h measurement.

10^6 atoms of ^{196}Au over approximately 152 laser shots [6]. In contrast, our experiment already demonstrates a significantly higher activation yield in a single shot, despite operating at 20 times lower peak intensity of approximately 10^{19} W/cm^2. Considering the differences in Au sample thickness, laser energy on target, and number of shots, we estimate an isotope yield of approximately 10^3 isotopes of ^{196}Au per joule of laser energy for LWFA (gas jet) and 2.5×10^5 for DLA (foam) at 20 times lower laser intensity.

The underlying acceleration mechanisms differ fundamentally between the two approaches. The ELI-NP experiment employs LWFA, which generates electrons with energies up to approximately 500 MeV but typically with relatively low charge. In contrast, our approach is based on DLA in overcritical-density foam targets, yielding electron energies up to approximately 100 MeV. However, this is accompanied by a substantially higher charge of the collimated fraction of DLA electrons, reaching 20 to 30 nC (for electrons with energies greater than 7.5 MeV).

Figure 5 displays the γ-ray spectrum of the irradiated converter material from the same shot (as in Fig. 4), composed of a 2-mm tantalum layer and a 1-mm gold layer, over the same energy range. In addition to the isotopes detected by the probes, this spectrum also reveals the presence of ^{190}Au and ^{174}Ta , which is notable given that their production requires incident x-rays with energies exceeding 55 MeV. The measured yield of ^{190}Au is $(1.62 \pm 0.02) \times 10^4$, and that of ^{174}Ta is $(5.03 \pm 0.05) \times 10^3$.

As expected, short-lived isotopes dominate in the initial measurement, whereas longer-lived isotopes become more apparent in the delayed measurement. The activity or yield of each isotope at the time of interaction is derived from the γ-ray spectra using the number of detected counts, detector efficiency, γ emission probabilities, duration of the measurement, and the elapsed time between irradiation and measurement start. The methodology for these calculations follows the approach outlined in Ref. [19,58].

To visualize the angular distribution of MeV photons, we employed the technique of autoradiography [48–50], using natural copper foils as activation targets. Copper was chosen specifically for its favorable nuclear properties: the (γ, n) reaction on ^{63}Cu produces the short-lived isotope ^{62}Cu, which has a half-life of 9.67 min. This moderate half-life provides a practical time window for postshot handling, as exposure to the IP must occur after the shot to avoid background interference, yet the sample must retain sufficient activity for readout.

Each copper foil had dimensions of 40×40 mm^2 and a thickness of 100 µm. At the center of each foil, tantalum (Ta) and gold (Au) probes were mounted, as previously described. Upon exposure to high-energy x-rays, the (γ, n) reaction in ^{63}Cu leads to the formation of ^{62}Cu, which decays predominantly via β^+ decay (approximately 97.83%) and, to a lesser extent, electron capture (approximately 2.17%), ultimately forming stable ^{62}Ni. The emitted positrons have a mean kinetic energy of 1320.7 keV, which can be detected using IPs to produce spatially resolved autoradiographs of the activated area.

After each shot, activated copper foils were exposed to BAS-IP MS for 15 min, allowing visualization of the MeV x-ray distribution in the 14- to 21-MeV range, corresponding to the FWHM of the ^{63}Cu (γ, n) ^{62}Cu reaction. The primary contributors to signals during contact imaging on the IP are β^+ particles (broad spectrum, 0–2936 keV, with a peak at 1320 keV), the characteristic gamma ray (1.17 MeV, $I_\gamma = 0.34\%$), and 511-keV photons from positron annihilation.

Taking into account the thickness of the protective layer (7 µm) and the thickness of the sensitive layer (115 µm) of the BAS-IP MS [59], along with the response functions of this IP type to photons and electrons or positrons [47], it is evident that the detection efficiency differs significantly between particle types. Specifically, the response is approximately 2×10^{-4} PSL per 511-keV photon and 4×10^{-2} PSL per incident 1.3-MeV electron or positron. Therefore, positrons that reach the sensitive layer are the primary contributors to the signal in the case of

100-μm-thin Cu foils. However, as the copper foil thickness increases, a larger fraction of positrons is annihilated within the copper before reaching the IP, resulting in an increased photon fluence. Consequently, for millimeter-thick copper layers, the dominant contribution to the IP signal shifts from positrons to photons [50]. A more detailed analysis based on GEANT4 simulations of positron transport and their contribution to the IP signal is provided in Appendix B, where it is also demonstrated how this approach can serve as an express method for estimating the number of 14–21-MeV photons based on the measured IP signal.

Figure 6 presents two exemplary autoradiography results: one for a shot directly on a 2-mm tungsten with a nanosecond prepulse, and another for a shot on preionized

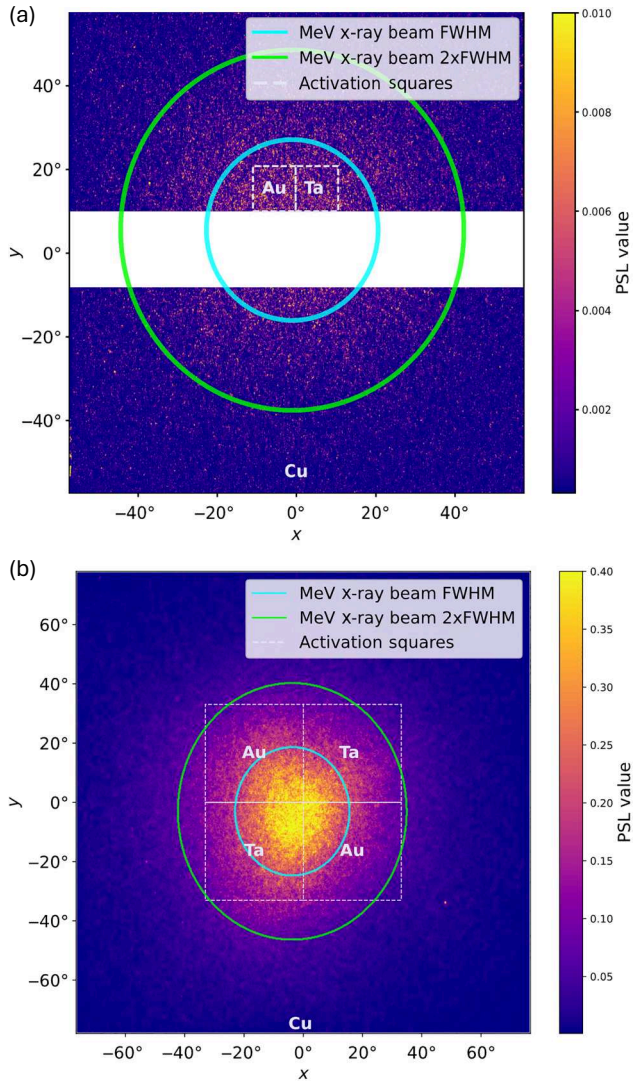

FIG. 6. Autoradiograph of x-rays passing through a 100-μm Cu foil: (a) for a shot directly on 2 mm W with an ns + ps laser pulse, and (b) for a shot on 15-mg cm^3 CHO + 2-mm Ta + 1-mm Au with an ns + ps laser pulse.

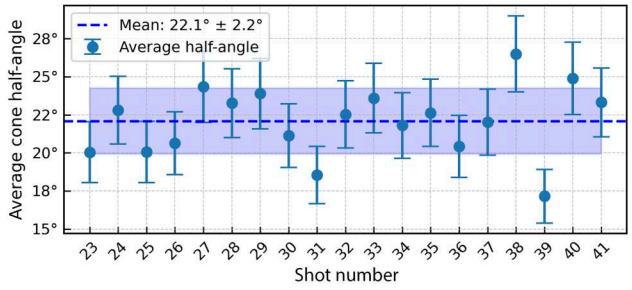

FIG. 7. Half-angle opening of the MeV photon beam for multiple shots, showing a highly stable average value of 22.1° ± 2.2°.

15-mg cm^{-3} CHO + 2-mm Ta + 1-mm Au. It is noticeable that, for the shot on the converter through the preionized foam target, the PSL signal value in the FWHM area is up to 40 times higher. The angular distribution of the MeV x-ray intensity was analyzed by fitting a two-dimensional Gaussian function to the spatial profiles obtained for each shot. From the fitted parameters, the half-angle opening of the MeV photon beam was determined. The autoradiographs also provided valuable information on the spatial irradiation of the Au and Ta probes placed behind the copper foils, enabling further calculations of the number of MeV photons in the beam.

The autoradiographs of 19 subsequent shots yielded an average cone half-angle of 22.1° ± 2.2°. Individual values for each shot, along with the average and its associated uncertainty, are presented in Fig. 7. The narrow spread

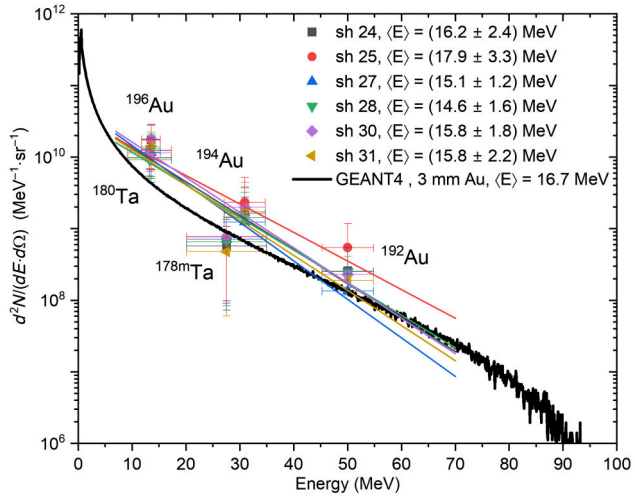

FIG. 8. Energy spectra of MeV x-ray radiation obtained from various shots using nuclear activation analysis. The solid lines represent linear fits over the 7- to 70-MeV energy range, with the corresponding average energies indicated in the legend. The black line shows the result of a GEANT4 simulation of MeV x-ray emission from the interaction of an electron beam with a 3-mm-thick gold converter.

TABLE I. Number of bremsstrahlung photons per steradian within the FWHM of the beam ($N_\gamma/\Omega_{1/2}$), mean photon energy above 7 MeV ($\langle E_\gamma\rangle_{>7\ \mathrm{MeV}}$), effective temperature (T_{eff}), solid angle corresponding to the FWHM opening angle of the photon beam ($\Omega_{1/2}$), and laser-to-photon conversion efficiency for photons above 7 MeV (η_γ) are presented for different experimental shots, together with their averaged values.

Shot No.	$N_\gamma/\Omega_{1/2}$ (sr^{-1})	$\langle E_\gamma\rangle_{>7\ \mathrm{MeV}}$ (MeV)	T_{eff} (MeV)	$\Omega_{1/2}$ (sr)	η_γ (%)
24	$(4.02 \pm 1.44) \times 10^{11}$	16.2 ± 2.4	9.2 ± 2.4	0.519 ± 0.156	1.35 ± 0.81
25	$(2.12 \pm 1.61) \times 10^{11}$	17.9 ± 3.3	10.9 ± 3.3	0.406 ± 0.128	1.36 ± 0.81
27	$(9.73 \pm 6.86) \times 10^{10}$	15.1 ± 1.2	8.1 ± 1.2	0.583 ± 0.167	1.41 ± 0.64
28	$(1.21 \pm 0.80) \times 10^{11}$	14.6 ± 1.6	7.6 ± 1.6	0.540 ± 0.158	1.13 ± 0.58
30	$(2.20 \pm 1.34) \times 10^{11}$	15.8 ± 1.8	8.8 ± 1.8	0.447 ± 0.136	1.34 ± 0.71
31	$(1.87 \pm 1.55) \times 10^{11}$	15.8 ± 2.2	8.8 ± 2.2	0.343 ± 0.108	0.80 ± 0.49
Mean ± Std.	$\mathbf{(2.07 \pm 1.08) \times 10^{11}}$	$\mathbf{15.90 \pm 1.13}$	$\mathbf{8.90 \pm 1.13}$	$\mathbf{0.473 \pm 0.090}$	$\mathbf{1.23 \pm 0.23}$

and consistency across shots demonstrate the good stability and reproducibility of MeV x-ray beam generation using preionized foam targets and a high-Z converter.

Figure 8 presents the differential bremsstrahlung photon fluence, $d^2N/dE\,d\Omega$, in the MeV range, reconstructed from the gamma-ray spectra of activated probes and autoradiographs over multiple shots. The results are shown alongside GEANT4 simulation data for comparison. Both the experimental data and the simulations correspond to the FWHM of the MeV x-ray beam profile. The spectra exhibit a consistent trend across all shots, with an average over six shots yielding a mean photon energy of 15.9 MeV for photons above 7 MeV. On average, the number of photons within the FWHM ($E > 7$ MeV) reaches $(2.07 \pm 1.08) \times 10^{11}$ photons/sr.

The uncertainty in determining the initial photon spectrum arises from the combined error in the measured reaction yields and the widths of the nuclear resonances relevant to each reaction [Figs. 3(a) and 3(b)].

The number of photons N_γ was estimated using the cross sections of (γ, xn) reactions (Fig. 3) at the FWHM value and considering the number of activations within the FWHM of the x-ray spot at photon energies of 14–20 MeV (Fig. 6). For the estimation of conversion efficiency, the mean photon energy $\langle E\rangle$ was obtained by integrating the bremsstrahlung spectrum between 7 and 70 MeV, while the laser energy on target was also taken at the FWHM of the laser energy distribution in the focal spot. In Table I the number of bremsstrahlung photons per steradian within the FWHM of the beam ($N_\gamma/\Omega_{1/2}$), mean photon energy above 7 MeV ($\langle E_\gamma\rangle_{>7\ \mathrm{MeV}}$), effective temperature (T_{eff}) from the $\log_{10}$-linear fit, solid angle corresponding to the FWHM opening angle of the MeV photon beam ($\Omega_{1/2}$), and laser-to-photon conversion efficiency for photons above 7 MeV (η_γ) are presented for different experimental shots, along with their average values.

To illustrate the impact of target configuration on laser-coupling efficiency to electrons—and, therefore, to bremsstrahlung generation—Fig. 9(a) shows the result of a laser shot on a bare Ta converter under high-contrast conditions. Only the roughness of the surface is visible, with no pronounced crater formation. The interaction appears to be dominated by surface ablation with limited coupling to the converter volume. Similarly, gamma spectroscopy did not reveal measurable production of Ta isotopes in this configuration, indicating that the bremsstrahlung spectrum generated was insufficient to induce photonuclear reactions such as (γ, xn). This observation is consistent with the electron spectrum obtained for the high-contrast shot [see Fig. 2(a), gray data points], which shows significantly lower electron energies and charge.

In contrast, Fig. 9(b) shows the crater formed when the Ta converter was irradiated through a 500-μm-thick overcritical-density CHO foam using a combined ps + ns pulse. This demonstrates a significantly increased coupling of laser energy to electrons, leading to surface melting and plasma formation. The 3D surface profile reveals two distinct crater regions: a sharply defined inner crater with an approximate diameter of 200 μm, surrounded by a broader outer depression extending approximately 1000 μm. The inner structure is attributed to the impact of collimated high-current DLA electrons propagating along the laser axis, while the outer crater is formed by more divergent electrons emitted into 2π. The maximum crater depth is approximately 500 μm. In this configuration—using a preionized foam target in front of the high-Z converter (2 mm Ta + 1 mm Au)—significant nuclear activation was observed in the converter; specifically, about 2×10^8 ^{196}Au isotopes were produced in the Au layer. Gamma spectroscopy also identified isotopes up to ^{190}Au (see Fig. 5). As this isotope requires bremsstrahlung photons with energies above 55 MeV, its presence confirms the generation of a high-energy tail in the photon spectrum.

As mentioned above, in this experiment, two bubble detectors were used to measure the number of neutrons produced per laser shot. The detectors recorded an average neutron fluence of 4.48×10^4 cm^{-2} along the axial direction (705 mm from the target) and 2.72×10^4 cm^{-2}

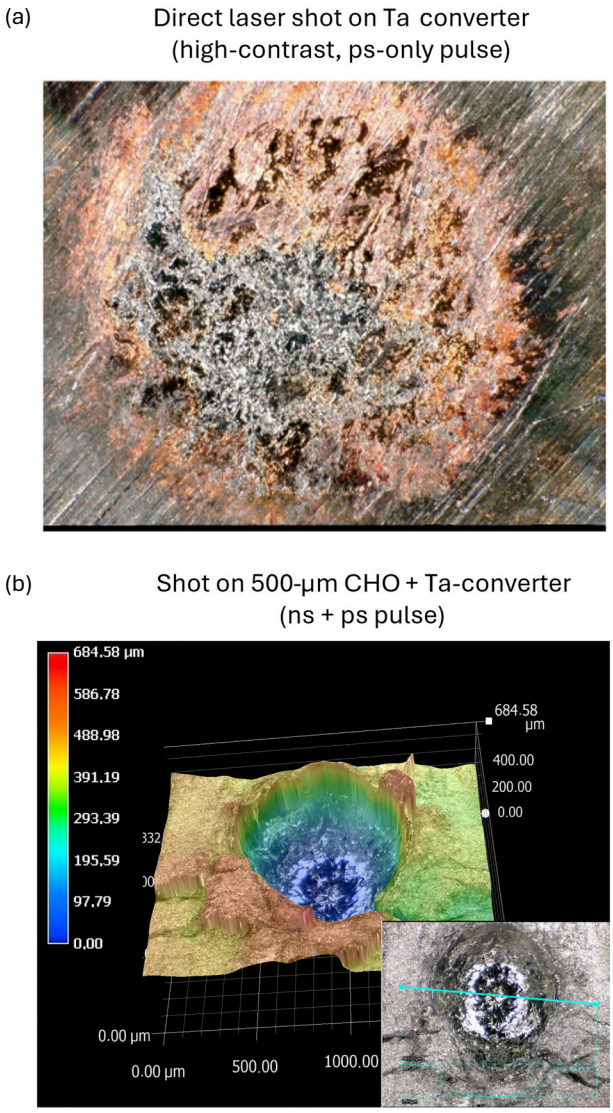

FIG. 9. Comparison of laser-induced modifications on the Ta target surface for two different irradiation configurations. (a) A high-contrast laser shot directly on a bare Ta converter shows only surface roughening without significant crater formation. (b) Irradiation through a 500-μm-thick CHO foam (15 mg cm^{-3}) using a combined ps + ns pulse leads to the formation of two distinct crater regions: a sharply defined inner crater surrounded by a broader, shallow crater region.

in the radial direction (670 mm from the target), indicating a nearly isotropic neutron distribution. Assuming that the neutrons originate primarily from the high-Z converter, these fluences correspond to an average total neutron yield of 2.7×10^9 (axial) and 1.7×10^9 (radial), as presented in Fig. 10. These values are in reasonable agreement with GEANT4 simulations for a 3-mm Au converter, which predict a neutron output of 8.4×10^8 [see Fig. 12(f)].

The duration of the neutron pulse is estimated to be less than 10 ps, based on the traverse time of 10–MeV electrons (the threshold for the photoneutron reaction)

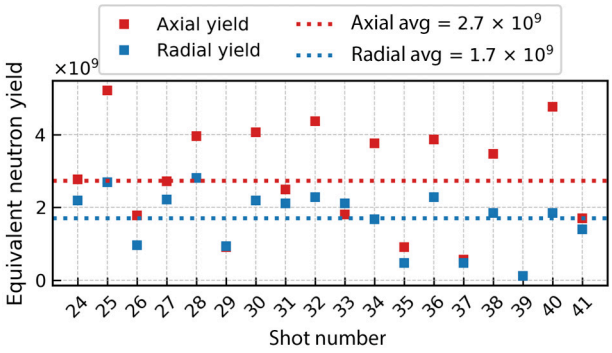

FIG. 10. Measured equivalent neutron yield per shot for axial and radial directions using bubble detectors. Dashed horizontal lines indicate the average yield for each direction: 2.7×10^9 neutrons (axial) and 1.7×10^9 neutrons (radial). The close agreement between the two values suggests a quasi-isotropic neutron emission.

through the 3-mm-thick high-Z converter. This pulse duration corresponds to a neutron flux peak of approximately 2×10^{20} n/cm^2/s, isotropically emitted into 4π sr. When normalized to the laser energy on target, this yields a flux of 4×10^{18} n/cm^2/s per joule at a laser intensity of 10^{19} W/cm^2.

For comparison, a neutron yield of approximately 1.2×10^9 with a peak flux of 1.1×10^{18} n/cm^2/s was reported in Ref. [18], where a laser of comparable energy but approximately 100 times higher intensity was used to drive superponderomotive electrons from an expanded polymer foil. In that study, an 18-mm Cu foil stack served as a converter for neutron production.

IV. MONTE CARLO SIMULATION OF BREMSSTRAHLUNG, POSITRON, AND NEUTRON PRODUCTION

To investigate in greater detail the interactions between DLA-accelerated electrons and the high-Z converter, Monte Carlo simulations were conducted to model bremsstrahlung generation, isotope production within the converter, and the associated neutron emission. The simulations presented in this study were performed using the Monte Carlo simulation toolkit GEANT4, version 10.1.2 [53]. Given the emphasis on modeling the interaction of MeV electrons with surrounding materials (resulting in the production of secondary photons, neutrons, and positrons), the QGSP_BERT_HP physics list was employed. This configuration incorporates the Bertini Intranuclear Cascade model, which provides detailed treatments of hadronic interactions and electromagnetic showers. The QGSP_BERT_HP list is recommended by the GEANT4 collaboration for applications involving medical and industrial neutron sources, as well as radiation shielding [60].

The input electron spectrum was derived from the experimental data shown in Fig. 2(c). To account for the directional distribution of the electron beam, a correction factor of 1.5 was applied to retrieve the number of electrons in the 0° direction, based on the angular profile measured using the cylindrical diagnostic [see Fig. 2(b)]. The electron beam exhibits a divergence characterized by a cone half-angle of 12.7° and was positioned 0.1 mm in front of the high-Z converter.

Gold plates with dimensions of 6×6 mm^2 and thicknesses of 0.1, 0.5, 1, 2, 3, 4, 5, 10, 20, and 50 mm were used as converters. The electron source was positioned at the center of the front face of the gold volume. Because of the prohibitively high computational cost of simulating the full number of electrons from the experiment, the number of electrons in the simulation was reduced to 10^7 particles. This reduction was accounted for in the final analysis by applying a normalization factor to the simulation results.

As electrons travel through matter, they lose energy mainly through inelastic (nonradiative) collisions and bremsstrahlung (radiative) processes. When their energy exceeds a certain threshold, known as the critical energy E_c, estimated by $E_c = 800/(Z + 1.2)$, where Z is the atomic number of the material, they can initiate an electromagnetic shower [61]. In this cascade, electrons, positrons, and photons continuously interact with the medium, losing energy in the process. The shower continues until the electron energy drops below E_c, after which nonradiative collisions again dominate. The bremsstrahlung photons produced during the shower, particularly those with energies above 7 MeV, can induce photonuclear reactions such as (γ, n). At photon energies below 30 MeV, the dominant mechanism for photoneutron production is giant dipole resonance, which is a collective excitation of the nucleus and results in nearly isotropic emission of neutrons with an evaporationlike energy spectrum [17].

Figure 11 shows the angular distribution of MeV x-rays in the energy range 10 to 21 MeV, evaluated at 10.6 mm from the electron source for the case of a 3-mm Au converter. The white dashed line indicates the FWHM of the distribution, which is approximately 32° (half-angle 16°). This result can be directly compared with the angular spread observed in Fig. 6(b) from the autoradiography measurements. The narrower divergence seen in the simulation arises from the fact that only forward-propagating electrons (within a cone of 12.7°) were included in the model. In contrast, the experiment includes a significant number of electrons with larger divergence outside this cone, resulting in a broader angular distribution in the measured data than in the simulation.

Figure 12 presents GEANT4-simulated energy spectra and conversion efficiencies for secondary particles produced by high-energy electrons incident on gold converters of various thicknesses (0.1 to 50 mm). The differential energy spectra ($\mathrm{d}N/\mathrm{d}E$) for bremsstrahlung photons, positrons, and neutrons are shown in Figs. 12(a)–12(c), respectively. As the converter thickness increases, the total yield of secondary particles generally rises, although the scaling behavior and saturation effects vary between particle species.

In Fig. 12(a), the bremsstrahlung photon yield increases with converter thickness up to 3 to 4 mm, beyond which attenuation effects occur. This trend is also reflected in Fig. 12(d), where both the number of MeV photons ($E >$ 7.5 MeV) and the associated conversion efficiency peak at 4 mm. For thicker converters, photon absorption and reduced transmission through the converter result in a decline in the overall photon yield. The diamond marker at a 3-mm converter thickness denotes the experimental measurement. Since the divergence at FWHM is known from the simulation (see Fig. 11), the conversion efficiency within this angular cone can be estimated. The resulting conversion efficiency of 1.7% (>7 MeV) is closely aligned with the experimental results (see Table I).

Figure 12(b) shows the energy spectra of the positrons, which display a marked increase in yield with increasing converter thickness due to enhanced pair production. Figure 12(e) shows that both the positron number ($E = 0.15$ to 90 MeV) and the conversion efficiency rise sharply up to approximately 5 mm before saturating. This plateau behavior is attributed to the limited escape probability of positrons from the deeper layers of the target. The maximum conversion efficiency of laser energy to positrons is achieved at 5 mm Au, reaching approximately 0.1%.

The neutron energy spectra in Fig. 12(c) show a Maxwell-Boltzmann-like shape with a pronounced peak

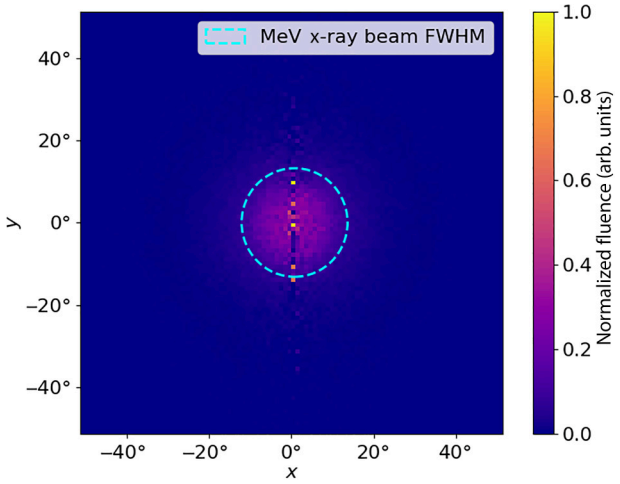

FIG. 11. Angular distribution of MeV x-rays ($14 < E <$ 21 MeV) generated from a 3-mm gold converter, as obtained from GEANT4 simulations. The distribution is shown in the x-y plane at a distance of 10.6 mm from the electron source. The white dashed line indicates a half-angle of 16° at FWHM.

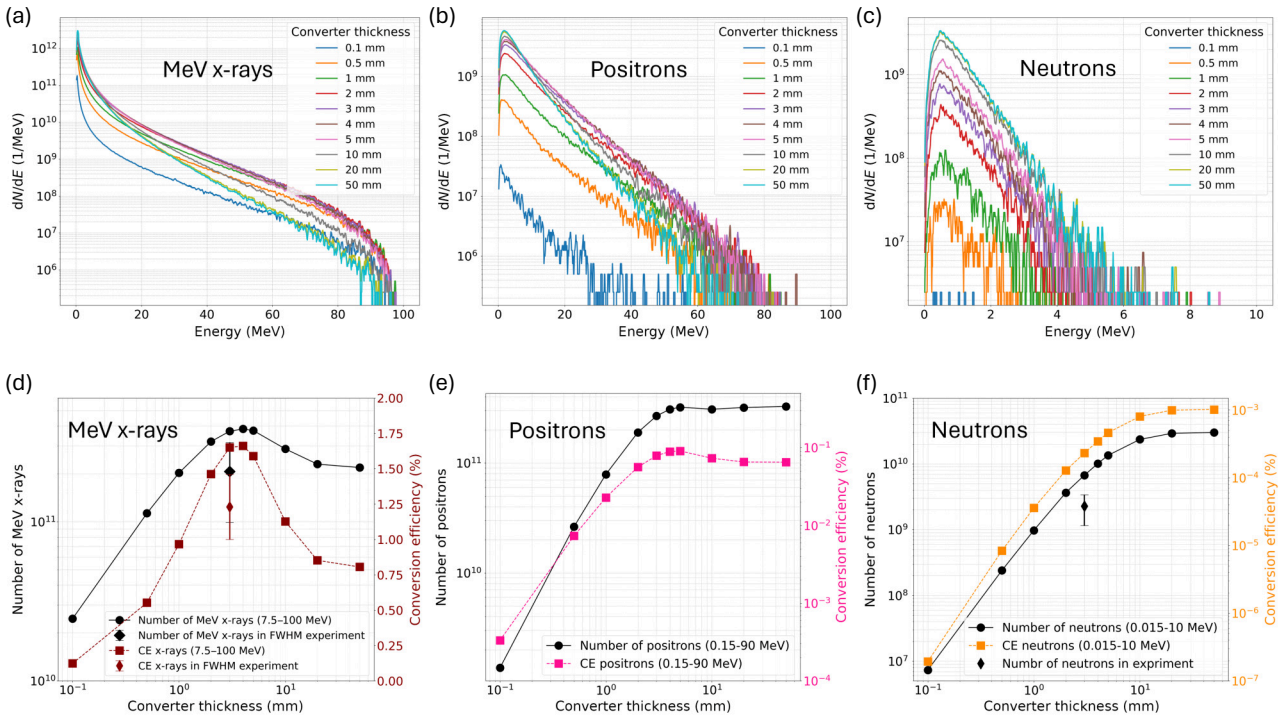

FIG. 12. GEANT4-simulated energy spectra and conversion characteristics of secondary particles produced in a gold converter of varying thickness (0.1–50 mm). Panels (a)–(c) show the differential number of emitted particles (dN/dE) as a function of energy for (a) bremsstrahlung photons, (b) positrons, and (c) neutrons. Panels (d)–(f) present the corresponding total number of particles (left axes) and conversion efficiency (right axes) as functions of converter thickness for (d) bremsstrahlung photons ($E = 7.5$–50 MeV), (e) positrons ($E = 0.15$–90 MeV), and (f) neutrons ($E = 0.01$–50 MeV).

around 1 MeV. This feature is attributed to neutron evaporation following nuclear de-excitation, primarily induced by the excitation of the GDR in gold nuclei through interactions with high-energy bremsstrahlung photons. The GDR produces a compound nucleus that subsequently emits neutrons with a characteristic energy spectrum in the MeV range. As shown in Fig. 12(f), both the neutron yield and the conversion efficiency increase with converter thickness, reaching a plateau at approximately 20 mm, where the maximum conversion efficiency is about 0.001%. This saturation suggests that most photonuclear reactions and the resulting neutron production take place within the first 2 cm of the converter. Beyond this point, attenuation of the primary photons significantly reduces further interaction.

In summary, the converter thickness has a pronounced, particle-specific influence on secondary particle production. For DLA electrons with an effective temperature of

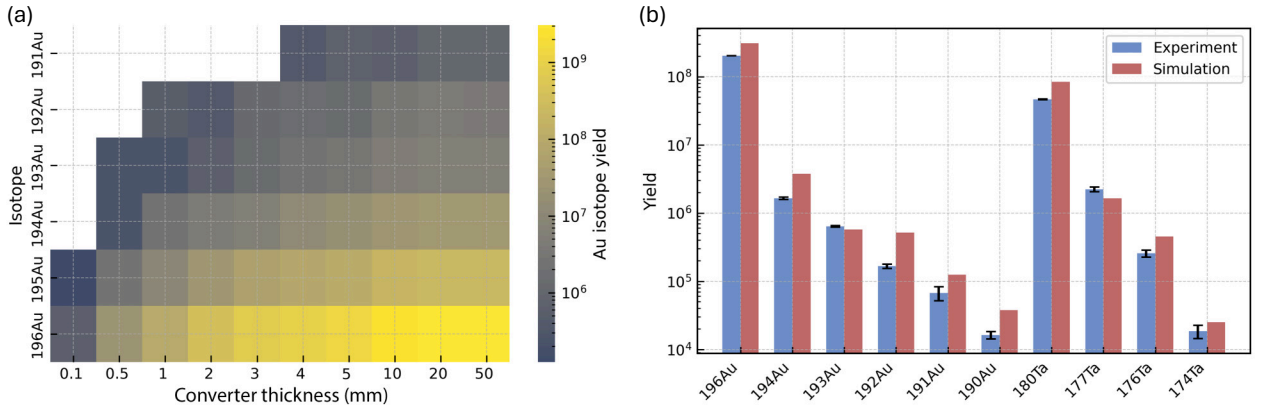

FIG. 13. (a) Heatmap of simulated gold isotope yields as a function of converter thickness. (b) Comparison of converter isotope yields of tantalum (2 mm) and gold (1 mm) in a selected shot and the corresponding GEANT4 simulation.

up to 30 MeV [Fig. 2(a)], an optimal thickness of around 3 to 4 mm maximizes the yield and efficiency of MeV x-rays. For positrons, 5 mm provides a good balance between production and escape, while neutron generation benefits from thicker targets (>20 mm) before reaching saturation. These findings provide guidance for optimizing the converter design based on the intended secondary particle application in future experimental campaigns. It is important to note that the optimal converter thickness depends on the effective electron temperature, which in turn depends on the laser intensity and the acceleration mechanism.

Bremsstrahlung photons with energies exceeding 7.5 MeV induce photonuclear reactions within the converter material, leading to the production of various isotopes. Figure 13(a) presents a heat map of the simulated gold isotope yields generated in the converter as a function of its thickness. The trend of the yield closely follows that of the neutron yield: up to 20 mm, the isotope yield increases significantly due to photonuclear reactions induced by MeV-range x-rays within the converter material. However, beyond this point, the yields begin to saturate, indicating that additional converter thickness contributes little to further activation. This saturation is due to the near-complete absorption of high-energy photons within the first few centimeters of the target, effectively limiting the depth at which photonuclear reactions can occur. In terms of experimental results, the 1-mm Au converter yielded 2×10^8 ^{196}Au isotopes. The corresponding simulation, estimated from the difference between the 2- and 3-mm Au converter cases, gives approximately 2.7×10^8 isotopes, which is consistent with the measured value.

In addition to the single-layer Au converters (0.1–50 mm thickness), we also investigated the experimentally used layered converter, consisting of 2 mm Ta followed by 1 mm Au. Figure 13(b) compares the isotope yields from the converter for a selected shot (the corresponding gamma-ray spectrum is shown in Fig. 5) with results from a dedicated simulation. The simulated yields are compared directly with the gamma-spectroscopy measurements for all isotopes identified in the converter. Overall, the simulated isotope yields agree well with the measured values.

Here we would like to emphasize once again that the converter thickness is optimized for the specific electron spectrum shown in Fig. 2(c) and may differ for other electron energy distributions.

V. CONCLUSION

We demonstrated ultrahigh conversion efficiency of laser energy into MeV-range bremsstrahlung x-rays through the interaction of DLA electrons with a high-Z converter, which is beyond 1%. The DLA process was driven by the 200-TW, subpicosecond PHELIX laser pulse at a moderately relativistic intensity of (1–2) 10^{19} W cm^{-2}, delivering approximately 60 J into a preionized foam target of initially overcritical density. As discussed in Ref. [46], a key requirement for effective laser interaction with such long-scale preionized plasma targets is the use of a high-f-number focusing optic ($f/5$ in the case of PHELIX).

The electron spectra from initially overcritical-density foam targets show a pronounced angular dependence. The highest effective temperatures, reaching 26–29 MeV with electron energies exceeding 100 MeV, were observed along the laser axis. By combining measurements from magnetic spectrometers and the cylindrical diagnostic, we estimated the total electron charge propagating within 2π as well as within the DLA emission cone: for electrons with energies above 1.5 MeV (the ponderomotive potential), the total charge was estimated to be around 300 nC; for electrons exceeding 7.5 MeV—sufficient to produce bremsstrahlung in the GDR region—the charge reached 80 to 100 nC in 2π and approximately 20 to 30 nC within the 12.7° half-angle beam cone.

Bremsstrahlung radiation in the MeV range, generated by DLA electrons in a 3-mm-thick high-Z converter, was investigated via activation analysis. For this purpose, two Au samples and two Ta samples, each 1 mm thick, were placed 1 cm from the converter and subsequently analyzed by gamma-ray spectroscopy of the characteristic gamma lines of the produced isotopes.

High activation yields were observed in a single laser shot and recorded by the two Au probes mounted on the activation grid: $(4.66 \pm 0.04) \times 10^7$ nuclei of ^{196}Au, $(5.35 \pm 0.29) \times 10^5$ nuclei of ^{194}Au and $(1.25 \pm 0.04) \times 10^5$ nuclei of ^{192}Au. The corresponding peak (γ, n) cross sections occur at approximately 14, 30, and 50 MeV, respectively. In addition, $(1.62 \pm 0.02) \times 10^4$ nuclei of ^{190}Au were measured directly in the converter target (two 1-mm Ta plates followed by a 1-mm Au plate). Production of ^{190}Au requires bremsstrahlung photons above 55 MeV, with the (γ, n) cross section peaking near 65 MeV. These results confirm the presence of an intense, broad-spectrum bremsstrahlung source extending to energies well above 50 MeV.

We estimated approximately 10^{11} photons per shot with energies between 7.5 and 70 MeV and an average energy of 15–18 MeV. The angular distribution of the 14–21-MeV gamma rays was determined by activation of the 100-μm-thin Cu plate and resulted in a $22° \pm 2°$ half-angle at FWHM. Considering a 10 ps x-ray pulse duration caused by relativistic electrons traversing the 3-mm converter, we arrive at an ultrahigh peak photon flux of approximately 2×10^{22} photons/sr/s together with a peak neutron flux of approximately 2×10^{20} n/cm^2/s at 10^{19}-W cm^{-2} laser intensity and 60-J laser energy on target.

Our experimental results are supported by GEANT4 simulations, which were used to optimize the converter

TABLE II. Summary of experimental parameters and resulting relativistic electron and MeV γ-ray production obtained on several high-intensity laser systems. The table compares target types, laser conditions, electron spectra, beam charge, and photon yields. Reported efficiencies are normalized to the laser energy on target.

Laser system I_{las} (W cm^{-2}) E_{las} (J), τ_{las} (ps) Reference	Target	Electrons E_{max} (MeV) T_{eff} (MeV) $\Omega_{1/2}$ (sr)	Beam charge Q_1 (nC) (>2 MeV) Q_2 (nC) (>7.5 MeV)	e^- efficiency Q_1/E_{las} (nC/J) Q_2/E_{las} (nC/J)	Photons N_γ (sr^{-1}) $\langle E \rangle$ (MeV) $\Omega_{1/2}$ (sr)	Photon efficiency N_γ/E_{las} (ph/J)
PHELIX (1–2)×10^{19} 60, 0.6 This work	500 µm CHO 15 mg cm^{-3} + 2 mm Ta + 1 mm Au + ns pulse	≥100 23–28 0.15	300 (Q_1) in 2π 100 (Q_1) directed 20–30 (Q_2) directed	 2 0.4	2.1 × 10^{11} (>7.5 MeV) 7–10 0.47	1.7 × 10^9 (>7.5 MeV)
Titan 2 × 10^{19} 120, 1 [62]	He gas jet 4 mm 2 × 10^{19} cm^{-3}	≥200 7–18 (T_1) 20–50 (T_2) 0.03	– 4–11 (Q_2)	– 0.1	10^{12} (<1 MeV) 0.8–2 0.15	2 × 10^9 (<1 MeV)
ARC 2 × 10^{18} 2400, 10 [3]	CPC + 2 mm Au	∼30 5–6 2π	500 (Q_1) 50 (Q_2) [in 2π, estimated from Fig. 3(a)]	0.2 0.02	5 × 10^{10} (>7.5 MeV) 2.5 2.2	2 × 10^9 (>7.5 MeV) (large divergence)
OMEGA 3.8 × 10^{19} 400, 1 [27]	CH foil + ps pulse 3 × 10^{18} cm^{-3}	∼500 33 0.1	140 (Q_1) –	0.35 –	– – –	– –
OMEGA 1.4 × 10^{19} 1500, 9 [63]	Ta (2 mm) + ns pulse	– – –	– –	– –	10^{12} (>7.5 MeV) – 1.8	3 × 10^9 (>7.5 MeV) (large divergence)
PETAL 8 × 10^{18} 450, 0.6 [33]	CH + Al + 5 ns ASE at 10^{-3}	40–50 8.3 –	300 (Q_1) –	0.7 –	– – –	– –

thickness and validate the photon and isotope production measured in the experiment. These simulations extend our findings by predicting the production of other secondary particles. Specifically, the simulations show a conversion efficiency of laser energy into MeV x-rays with $E > 7.5$ MeV of 1.7% (3-mm Au, within the FWHM of the beam), and 0.1% into positrons, achieved at relativistically moderate laser intensity. These values are more than 10 times higher than in Ref. [64], where conversion efficiencies of approximately 0.2% for gamma rays ($E >$ 1 MeV) and 0.002% for positrons were observed using conventional foil targets and kJ petawatt-class laser systems.

To place our results in a broader context, Table II compares our measurements with previous experiments on relativistic electron and MeV bremsstrahlung generation across various (sub-)PW and (sub-)kJ laser facilities. As highlighted in previous studies, (sub)picosecond laser-plasma interactions can drive different acceleration mechanisms: SM-LWFA, hybrid SM-LWFA + DLA, or predominantly DLA, depending on the target configuration. The comparison of beam charge and MeV photon yield per joule of laser energy demonstrates that DLA in preionized low-density foams (this work) offers a clear advantage over gas jets and solid targets.

To further support these findings, we note that 3D PIC simulations predict a linear scaling of electron-beam charge with laser energy at constant intensity. This scaling behavior will be tested in dedicated experiments scheduled at the ARC and PETAL facilities in 2026 and 2027.

The robustness of DLA in preionized foam targets, together with the ultrahigh efficiency of MeV bremsstrahlung and isotope production demonstrated in experiments at PHELIX, paves the way for a wide range of applications of foams in high-energy-density physics and nuclear astrophysics research with intense lasers.

ACKNOWLEDGMENTS

This work was funded by the German Ministry of Education and Research (BMBF) under Contract No. 05P21SJFA2. The work of the authors affiliated with CTU was supported by the Czech Science Foundation

(Project No. GM23-05027M). The results presented here are part of experiment No. P21-00005, conducted at the PHELIX facility at GSI Helmholtzzentrum für Schwerionenforschung in Darmstadt, Germany, during April/May 2023 within the framework of FAIR Phase-0. The authors specifically thank the PHELIX laser team at GSI for their dedicated support in carrying out the experimental campaign, as well as to the GSI Plasma Physics Department and the Group for Safety and Waste Management. The authors gratefully acknowledge Prof. Sergey Yu. Gus'kov and Dr. Rafael Yakhin for performing hydrodynamic simulations of the ns-pulse interaction with overcritical foam targets, and Dr. Wigen Nazarov for providing the foam targets used in this study.

DATA AVAILABILITY

The data that support the findings of this article are openly available [65].

APPENDIX A: NUCLEAR REACTION DATA

Nuclear reaction data for the photonuclear reaction in gold and tantalum are listed in Tables III and IV. These tables primarily list the threshold energies for different photonuclear reactions, the half-lives of the resulting daughter nuclides, their decay modes, and the most intense gamma-ray lines of various gold and tantalum isotopes. However, not all expected isotopes could be observed because of either their extremely long half-lives or unfavorable gamma-ray emission characteristics.

APPENDIX B: SIMULATION OF POSITRON TRANSPORT AND PHOTON YIELD ESTIMATION

The transport of positrons, produced due to β^+ emission from the decaying ^{62}Cu isotopes created inside the copper sample, through the IP was simulated using the Monte Carlo code GEANT4 [53].

For these simulations, a copper box of dimensions $15 \times 15 \times 0.1$ mm^3 was used. The positrons were assumed to originate from a cylindrical volume with a radius of 7.5 mm and a height that corresponds to the thickness of the Cu plate, i.e., 0.1 mm. The cylindrical geometry was chosen to better represent the geometry of the laser beam and the electron and gamma-ray beams it produced. The positrons were evenly distributed within this volume. Their angular distribution was assumed to be isotropic, and their initial energies were defined based on the available β^+-decay spectrum data for ^{62}Cu, which was taken from the MCNP code [66].

A total of 10^5 particles (5.66×10^6 positrons per cm^3) were simulated, and their resulting energy spectrum at the position of the IP, located at one edge of the copper sample, was recorded. To avoid boundary effects, only positrons propagating close to the center of the box were considered, where their distribution was sufficiently uniform, thus minimizing the influence of edge artifacts.

Figure 14 shows the unperturbed input positron energy spectrum, as well as the positron energy spectrum propagating through the 0.1-mm-thick copper sample and exiting on the opposite side.

TABLE III. Nuclear reaction data for the photonuclear reaction in gold.

Reaction channel	Threshold (MeV)	Reaction max. (MeV)	Max. σ (mb)	Half-life	Decay mode	Energy (keV)	Intensity (%)
$^{197}_{79}\mathrm{Au}(\gamma,n)^{196}_{79}\mathrm{Au}$	8.1	14.1	398	6.167 d	EC + β^+ = 93%, β^- = 7%	355.7	87
						333.0	22.9
						426.1	6.6
$^{197}_{79}\mathrm{Au}(\gamma,2n)^{195}_{79}\mathrm{Au}$	14.7	17.1	126.6	186.01 d	EC (100%)	98.9	11.2
$^{197}_{79}\mathrm{Au}(\gamma,3n)^{194}_{79}\mathrm{Au}$	23.1	30.1	18.5	38.02 h	EC + β^+ = 100%	328.5	62.8
						293.5	10.9
						1468.9	6.8
$^{197}_{79}\mathrm{Au}(\gamma,4n)^{193}_{79}\mathrm{Au}$	30.0	40.1	12.0	17.65 h	EC + β^+ = 100%	186.2	9.7
						255.6	6.5
						268.2	3.8
$^{197}_{79}\mathrm{Au}(\gamma,5n)^{192}_{79}\mathrm{Au}$	38.7	49.1	8.1	4.94 h	EC + β^+ = 100%	316.5	59.0
						296.0	23
						2237.3	4.7
$^{197}_{79}\mathrm{Au}(\gamma,6n)^{191}_{79}\mathrm{Au}$	45.8	58.1	7.2	3.18 h	EC + β^+ = 100%	586.4	14.0
						277.9	5.9
						674.2	5.6
$^{197}_{79}\mathrm{Au}(\gamma,7n)^{190}_{79}\mathrm{Au}$	54.8	66.1	5.1	42.8 min	EC + β^+ = 100%	295.8	90
						301.8	30
						597.7	12.0

TABLE IV. Nuclear reaction data for the photonuclear reaction in tantalum.

Reaction channel	Threshold (MeV)	Reaction max. (MeV)	Max. σ (mb)	Half-life	Decay mode	Energy (keV)	Intensity (%)
$^{181}_{73}\mathrm{Ta}(\gamma,n)^{180}_{73}\mathrm{Ta}$	7.6	12.5	346	8.15 h	EC (85%), β^- (15%)	93.3	11
						215.4	6.5
$^{181}_{73}\mathrm{Ta}(\gamma,2n)^{179}_{73}\mathrm{Ta}$	14.2	16	203	1.82 y	EC (100%)		
$^{181}_{73}\mathrm{Ta}(\gamma,3n)^{178\mathrm{m}_{73}Ta}$	22.0	26	8.9	2.36 h	EC + β^+ = 100%	213.4	81.4
						325.6	94
						331.6	31.2
						426.4	97
$^{181}_{73}\mathrm{Ta}(\gamma,4n)^{177}_{73}\mathrm{Ta}$	31.2	38	10.5	56.56 h	EC + β^+ = 100%	112.9	11.4
						208.4	1.5
						1159.3	24.7
$^{181}_{73}\mathrm{Ta}(\gamma,5n)^{176}_{73}\mathrm{Ta}$	39.1	46	7.2	8.09 h	EC + β^+ = 100%	201.8	5.7
						1225.0	5.7
						710.5	5.4
$^{181}_{73}\mathrm{Ta}(\gamma,6n)^{175}_{73}\mathrm{Ta}$	44.5	55	6.8	10.5 h	EC + β^+ = 100%	207.4	14.0
						348.5	12.0
						266.9	10.8
$^{181}_{73}\mathrm{Ta}(\gamma,7n)^{174}_{73}\mathrm{Ta}$	53.2	63	5.2	1.14 h	EC + β^+ = 100%	206.5	60.0
						91.0	15.9
						1205.9	4.9

The simulation results indicate that, for a 0.1-mm-thick copper sample, the energy spectrum of the positrons does not undergo substantial modification. The spectral peak shifts slightly toward lower energies, and the number of high-energy positrons is reduced. The resulting energy spectrum at the IP position can be used to estimate the corresponding signal. To this end, the spectrum is convolved with the response function of the MS-type IP to electrons, as extracted from Ref. [47].

The signal level of the IP depends on the density of the positrons. The latter can then be scaled to obtain an estimate of the density that is required to produce a signal of 1 PSL. The resulting value, i.e., the initial positron density, which corresponds to the IP signal of 1 PSL, is

$$R = 1.38 \times 10^8 \ \mathrm{positrons/cm^3}.$$

This dependence of the IP signal on the density of the positron can be used to estimate the fluence of photons in the energy range between 14 and 21 MeV:

$$N_{e^+} = RV_{\mathrm{PSL}} = N_\gamma \sigma n_{\mathrm{Cu}}. \tag{B1}$$

Here, N_{e^+} is the positron density, N_γ is the photon number density per unit area, V_{PSL} is the signal measured by the image plate in PSL (at the FWHM level), $\sigma \simeq 0.04 \times 10^{-24}\ \mathrm{cm^2}$ is the reaction cross section of $^{63}\mathrm{Cu}(\gamma,n)^{62}\mathrm{Cu}$, and $n_{\mathrm{Cu}} \approx 8.5 \times 10^{22}\ \mathrm{cm^{-3}}$ is the number density of copper atoms.

The gamma-photon flux is then given by

$$N_\gamma = D\frac{RV_{\mathrm{PSL}}}{\sigma n_{\mathrm{Cu}}}, \tag{B2}$$

where an additional factor $D = N^0_{\mathrm{Cu}}/\Delta N_{\mathrm{Cu}}$ has been introduced to account for the exponential decay of ^{62}Cu isotopes:

$$\Delta N_{\mathrm{Cu}} = N^0_{\mathrm{Cu}}(e^{-(t_1 \ln 2)/T_{1/2}} - e^{-(t_2 \ln 2)/T_{1/2}}). \tag{B3}$$

Here, ΔN_{Cu} is the number of copper isotopes that decay through positron emission during exposure time, N^0_{Cu} is the initial isotope concentration immediately after the shot, t_1 is the time between the shot and the start of exposure, and t_2 is the time between the shot and the end of exposure.

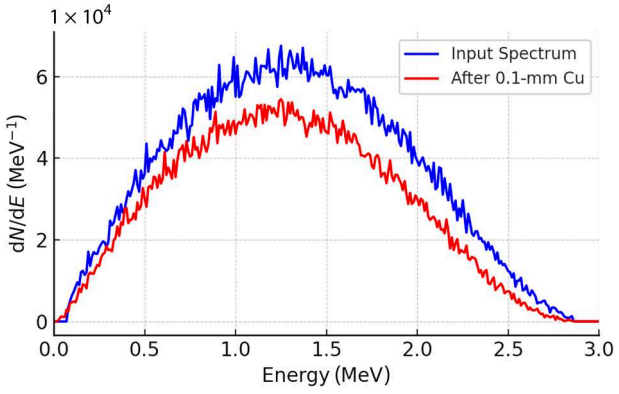

FIG. 14. Unperturbed positron spectrum used as an input to the simulation (blue line) and the spectrum created by positrons propagating through the 0.1-mm-thick copper sample and exiting on the opposite side (red line).

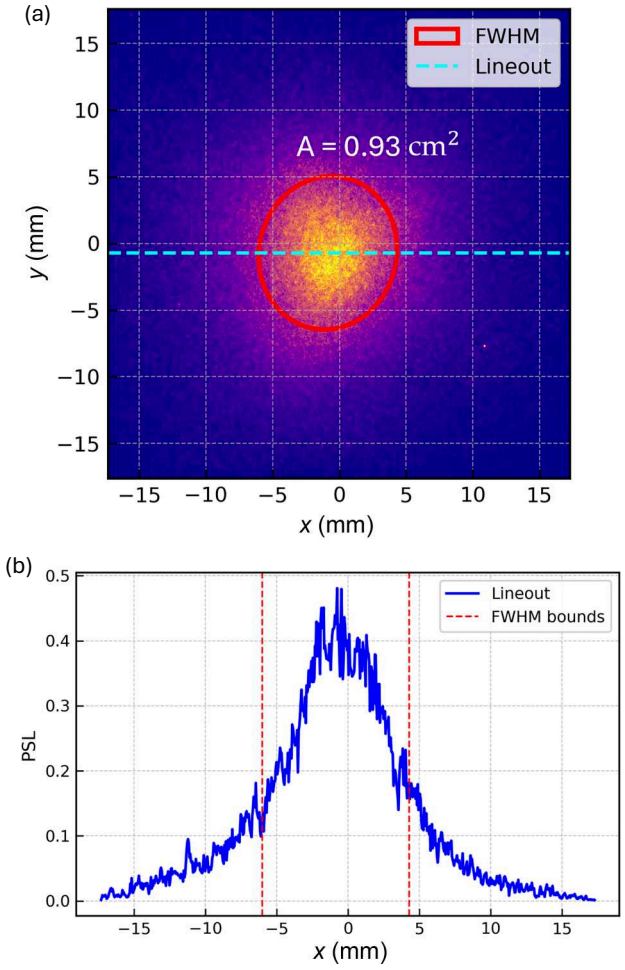

FIG. 15. (a) Autoradiography result of shot 24. IP signal showing the spatial distribution of ^{62}Cu activity. The red circle marks the region corresponding to FWHM. The dashed cyan line indicates the horizontal lineout used for analysis. (b) Horizontal lineout profile of the PSL signal, with vertical dashed red lines indicating the FWHM bounds.

An example of this approach is shown in Fig. 15, which presents the autoradiography result of shot 24, with a measured signal of $V_{\mathrm{PSL}} \approx 0.2$ and a correction factor $D \approx 45$. Substituting these values into Eq. (B2) yields a photon fluence of approximately $3.6 \times 10^{11}\,\mathrm{cm}^{-2}$. Given a beam area of $S \approx 0.93\,\mathrm{cm}^2$, this corresponds to a total of 3.5×10^{11} photons within the FWHM of the bremsstrahlung beam.

This estimate is consistent with the result shown in Fig. 8, which displays the photon spectrum for shot 24. There, the number of photons in the 14–21-MeV range per unit solid angle is $5.7 \times 10^{11}\,\mathrm{sr}^{-1}$, and the FWHM solid angle is $\Omega_{1/2} = 0.533\,\mathrm{sr}$, leading to an estimated total of 3.0×10^{11} photons.

This express technique serves as a practical and efficient alternative for estimating high-energy photon yields between subsequent laser shots, particularly when the conventional isotope-counting method based on Eq. (1) is experimentally demanding and time-intensive. However, it should be noted that the method provides reliable results only for copper targets with thicknesses of the order of millimeters. For centimeter-thick samples, the dominant contribution to the image plate signal arises from 511-keV photons produced by positron annihilation [50].

[1] K. W. D. Ledingham and W. Galster, Laser-driven particle and photon beams and some applications, New J. Phys. **12**, 045005 (2010).

[2] D. Habs and U. Köster, Production of medical radioisotopes with high specific activity in photonuclear reactions with γ-beams of high intensity and large brilliance, Appl. Phys. B **103**, 501 (2011).

[3] S. M. Kerr *et al.*, Development of a bright MeV photon source with compound parabolic concentrator targets on the National Ignition Facility Advanced Radiographic Capability (NIF-ARC) laser, Phys. Plasmas **30**, 013101 (2023).

[4] D. P. Broughton, S. Palaniyappan, C.-K. Huang, N. R. C. Lemos, A. MacKinnon, A. Pak, P. K. Singh, C.-S. Wong, M. Alvarado Alvarez, S. R. Klein, A. Junghans, S. H. Batha, R. E. Reinovsky, and A. Favalli, Laser-driven flash x-ray radiography of a shocked metallic foil, AIP Adv. **15**, 055023 (2025).

[5] D. Ursescu, G. Chériaux, P. Audebert, M. Kalashnikov, T. Toncian, M. Cherchez, M. Kaluza, G. Paulus, G. Priebe, R. Dabu, M. O. Cernaianu, M. Dinescu, T. Asavei, I. Dancus, L. Neagu, B. Boianu, C. Hooker, C. Barty, and C. Haefner, Laser driven nuclear physics at ELI-NP, Rom. Rep. Phys. **68**, S11 (2016).

[6] G. Giubega *et al.*, Preliminary results on nuclear isomer production via laser-driven bremsstrahlung irradiation at ELI-NP-1PW, Nucl. Phys. A **1062**, 123157 (2025).

[7] D. L. Balabanski and W. Luo, Nuclear photonics and nuclear isomers, Eur. Phys. J. Spec. Top. **233**, 1161 (2024).

[8] P. Mohr, Z. Fülöp, and H. Utsunomiya, Photo-induced nucleosynthesis: Current problems and experimental approaches, Eur. Phys. J. A **32**, 357 (2007).

[9] M. Mirzaie, C. I. Hojbota, D. Y. Kim, V. B. Pathak, T. G. Pak, C. M. Kim, H. W. Lee, J. W. Yoon, S. K. Lee, Y. J. Rhee, M. Vranic, Ó. Amaro, K. Y. Kim, J. H. Sung, and C. H. Nam, All-optical nonlinear compton scattering performed with a multi-petawatt laser, Nat. Photonics **18**, 1212 (2024).

[10] M. A. Stoyer, T. C. Sangster, E. A. Henry, M. D. Cable, T. E. Cowan, S. P. Hatchett, M. H. Key, M. J. Moran, D. M. Pennington, M. D. Perry, T. W. Phillips, M. S. Singh, R. A. Snavely, M. Tabak, and S. C. Wilks, Nuclear diagnostics for petawatt experiments (invited), Rev. Sci. Instrum. **72**, 767 (2001).

[11] I. Spencer, K. W. D. Ledingham, R. P. Singhal, T. McCanny, P. Mckenna, E. L. Clark, K. Krushelnick, M. Zepf, F. N. Beg, M. Tatarakis, A. E. Dangor, R. D. Edwards, M. A. Sinclair, P. A. Norreys, R. J. Clarke, and R. M. Allott, A nearly real-time high temperature laser–plasma

diagnostic using photonuclear reactions in tantalum, Rev. Sci. Instrum. **73**, 3801 (2002).

[12] R. D. Edwards, M. A. Sinclair, T. J. Goldsack, K. Krushelnick, F. N. Beg, E. L. Clark, A. E. Dangor, Z. Najmudin, M. Tatarakis, B. Walton, M. Zepf, K. W. D. Ledingham, I. Spencer, P. A. Norreys, R. J. Clarke, R. Kodama, Y. Toyama, and M. Tampo, Characterization of a gamma-ray source based on a laser-plasma accelerator with applications to radiography, Appl. Phys. Lett. **80**, 2129 (2002).

[13] A. Pukhov and J. Meyer-ter Vehn, Laser wake field acceleration: the highly non-linear broken-wave regime, Appl. Phys. B **74**, 355 (2002).

[14] S. Corde, K. Ta Phuoc, G. Lambert, R. Fitour, V. Malka, A. Rousse, A. Beck, and E. Lefebvre, Femtosecond x rays from laser-plasma accelerators, Rev. Mod. Phys. **85**, 1 (2013).

[15] V. Malka, J. Faure, Y. A. Gauduel, E. Lefebvre, A. Rousse, and K. T. Phuoc, Principles and applications of compact laser–plasma accelerators, Nat. Phys. **4**, 447 (2008).

[16] J. M. Cole, J. C. Wood, N. C. Lopes, K. Poder, R. L. Abel, S. Alatabi, J. S. J. Bryant, A. Jin, S. Kneip, K. Mecseki, D. R. Symes, S. P. D. Mangles, and Z. Najmudin, Laser-wakefield accelerators as hard x-ray sources for 3D medical imaging of human bone, Sci. Rep. **5**, 13244 (2015).

[17] B. L. Berman and S. C. Fultz, Measurements of the giant dipole resonance with monoenergetic photons, Rev. Mod. Phys. **47**, 713 (1975).

[18] I. Pomerantz, E. McCary, A. R. Meadows, A. Arefiev, A. C. Bernstein, C. Chester, J. Cortez, M. E. Donovan, G. Dyer, E. W. Gaul, D. Hamilton, D. Kuk, A. C. Lestrade, C. Wang, T. Ditmire, and B. M. Hegelich, Ultrashort pulsed neutron source, Phys. Rev. Lett. **113**, 184801 (2014).

[19] M. M. Günther, O. N. Rosmej, P. Tavana, M. Gyrdymov, A. Skobliakov, A. Kantsyrev, S. Zähter, N. G. Borisenko, A. Pukhov, and N. E. Andreev, Forward-looking insights in laser-generated ultra-intense γ-ray and neutron sources for nuclear application and science, Nat. Commun. **13**, 170 (2022).

[20] Christian Segebade, Hans-Peter Weise, and George John Lutz, *Photon Activation Analysis* (Walter de Gruyter, Berlin, 2011).

[21] F. Mirani, D. Calzolari, A. Formenti, and M. Passoni, Superintense laser-driven photon activation analysis, Commun. Phys. **4**, 185 (2021).

[22] N. E. Andreev, L. M. Gorbunov, V. I. Kirsanov, A. A. Pogosova, and R. R. Ramazashvili, The theory of laser self-resonant wake field excitation, Phys. Scr. **49**, 101 (1994).

[23] N. E. Andreev, V. I. Kirsanov, and L. M. Gorbunov, Stimulated processes and self-modulation of a short intense laser pulse in the laser wake-field accelerator, Phys. Plasmas **2**, 2573 (1995).

[24] W. B. Mori, C. D. Decker, D. E. Hinkel, and T. Katsouleas, Raman forward scattering of short-pulse high-intensity lasers, Phys. Rev. Lett. **72**, 1482 (1994).

[25] F. Albert, N. Lemos, J. L. Shaw, B. B. Pollock, C. Goyon, W. Schumaker, A. M. Saunders, K. A. Marsh, A. Pak, J. E. Ralph, J. L. Martins, L. D. Amorim, R. W. Falcone, S. H. Glenzer, J. D. Moody, and C. Joshi, Observation of betatron x-ray radiation in a self-modulated laser wakefield accelerator driven with picosecond laser pulses, Phys. Rev. Lett. **118**, 134801 (2017).

[26] N. Lemos, F. Albert, J. L. Shaw, D. Papp, R. Polanek, P. King, A. L. Milder, K. A. Marsh, A. Pak, B. B. Pollock, B. M. Hegelich, J. D. Moody, J. Park, R. Tommasini, G. J. Williams, H. Chen, and C. Joshi, Bremsstrahlung hard x-ray source driven by an electron beam from a self-modulated laser wakefield accelerator, Plasma Phys. Controlled Fusion **60**, 054008 (2018).

[27] A. E. Hussein, A. V. Arefiev, T. Batson, H. Chen, R. S. Craxton, A. S. Davies, D. H. Froula, Z. Gong, D. Haberberger, Y. Ma, P. M. Nilson, W. Theobald, T. Wang, K. Weichman, G. J. Williams, and L. Willingale, Towards the optimisation of direct laser acceleration, New J. Phys. **23**, 023031 (2021).

[28] N. Lemos, P. M. King, D. Rusby, I. Pagano, M. Sinclair, K. A. Marsh, J. L. Shaw, A. L. Milder, A. Pak, B. B. Pollock, M. Aufderheide, F. V. Hartemann, S. Q. Wu, Y. Hwang, B. M. Hegelich, J. Moody, P. Michel, C. Joshi, and F. Albert, Ultrabroad-band x-ray source using a picosecond, laser-driven plasma accelerator, Phys. Rev. Res. **6**, L032022 (2024).

[29] P. M. King, N. Lemos, J. L. Shaw, A. L. Milder, K. A. Marsh, A. Pak, B. M. Hegelich, P. Michel, J. Moody, C. Joshi, and F. Albert, X-ray analysis methods for sources from self-modulated laser wakefield acceleration driven by picosecond lasers, Rev. Sci. Instrum. **90**, 033503 (2019).

[30] W. Cayzac *et al.*, Experimental capabilities of the LMJ-PETAL facility, High Energy Density Phys. **52**, 101125 (2024).

[31] J. L. Shaw, M. A. Romo-Gonzalez, N. Lemos, P. M. King, G. Bruhaug, K. G. Miller, C. Dorrer, B. Kruschwitz, L. Waxer, G. J. Williams, M. V. Ambat, M. M. McKie, M. D. Sinclair, W. B. Mori, C. Joshi, H. Chen, J. P. Palastro, F. Albert, and D. H. Froula, Microcoulomb ($0.7 \pm \frac{0.4}{0.2}$ μC) laser plasma accelerator on OMEGA EP, Sci. Rep. **11**, 7498 (2021).

[32] G. J. Williams *et al.*, Order-of-magnitude increase in laser-target coupling at near-relativistic intensities using compound parabolic concentrators, Phys. Rev. E **103**, L031201 (2021).

[33] D. Raffestin, L. Lecherbourg, I. Lantuéjoul, B. Vauzour, P. E. Masson-Laborde, X. Davoine, N. Blanchot, J. L. Dubois, X. Vaisseau, E. d'Humières, L. Gremillet, A. Duval, C. Reverdin, B. Rosse, G. Boutoux, J. E. Ducret, C. Rousseaux, V. Tikhonchuk, and D. Batani, Enhanced ion acceleration using the high-energy petawatt PETAL laser, Matter Radiat. Extremes **6**, 056901 (2021).

[34] N. G. Borisenko, I. V. Akimova, A. I. Gromov, A. M. Khalenkov, Y. A. Merkuliev, V. N. Kondrashov, J. Limpouch, J. Kuba, E. Krousky, K. Masek, W. Nazarov, and V. G. Pimenov, Regular 3-D networks with clusters for controlled energy transport studies in laser plasma near critical density, Fusion Sci. Technol. **49**, 676 (2006).

[35] O. N. Rosmej, N. E. Andreev, S. Zaehter, N. Zahn, P. Christ, B. Borm, T. Radon, A. Sokolov, L. P. Pugachev, D. Khaghani, F. Horst, N. G. Borisenko, G. Sklizkov, and V. G. Pimenov, Interaction of relativistically intense laser pulses with long-scale near critical plasmas for optimization of laser based sources of MeV electrons and gamma-rays, New J. Phys. **21**, 043044 (2019).

[36] O. N. Rosmej, M. Gyrdymov, M. M. Günther, N. E. Andreev, P. Tavana, P. Neumayer, S. Zähter, N. Zahn, V. S. Popov, N. G. Borisenko, A. Kantsyrev, A. Skobliakov, V. Panyushkin, A. Bogdanov, F. Consoli, X. F. Shen, and A. Pukhov, High-current laser-driven beams of relativistic electrons for high energy density research, Plasma Phys. Controlled Fusion **62**, 115024 (2020).

[37] A. Pukhov, Z.-M. Sheng, and J. Meyer-ter-Vehn, Particle acceleration in relativistic laser channels, Phys. Plasmas **6**, 2847 (1999).

[38] A. Pukhov, Strong field interaction of laser radiation, Rep. Prog. Phys. **66**, 47 (2003).

[39] M. Gyrdymov *et al.*, High-brightness betatron emission from the interaction of a sub picosecond laser pulse with pre-ionized low-density polymer foam for ICF research, Sci. Rep. **14**, 14785 (2024).

[40] J. Cikhardt, M. Gyrdymov, S. Zähter, P. Tavana, M. M. Günther, N. Bukharskii, N. Borisenko, J. Jacoby, X. F. Shen, A. Pukhov, N. E. Andreev, and O. N. Rosmej, Characterization of bright betatron radiation generated by direct laser acceleration of electrons in plasma of near critical density, Matter Radiat. Extremes **9**, 027201 (2024).

[41] P. Tavana, N. Bukharskii, M. Gyrdymov, U. Spillmann, Ş. Zähter, J. Cikhardt, N. G. Borisenko, P. Korneev, J. Jacoby, C. Spielmann, N. E. Andreev, M. M. Günther, and O. N. Rosmej, Ultra-high efficiency bremsstrahlung production in the interaction of direct laser-accelerated electrons with high-Z material, Front. Phys. **11**, 1178967 (2023).

[42] R. Kalla, P. Boller, P. Tavana, C. Brabetz, J. Burggraf, J. Cikhardt, J. Glorius, M. Gyrdymov, Y. A. Litvinov, W. Nazarov, J. Novotny, U. Spillmann, D. H. G. Schneider, A. Yakushev, A. Zylstra, O. N. Rosmej, T. Kuehl, and V. Bagnoud, On-shot detection of fission isotopes of ^{238}U, produced by laser-driven x-rays, Phys. Plasmas **32**, 073106 (2025).

[43] V. Bagnoud *et al.*, Commissioning and early experiments of the PHELIX facility, Appl. Phys. B **100**, 137 (2010).

[44] Z. Major *et al.*, High-energy laser facility PHELIX at GSI: Latest advances and extended capabilities, High Power Laser Sci. Eng. **12**, e39 (2024).

[45] S. Y. Gus'kov and R. A. Yakhin, Nonstationary laser-supported ionization wave in layer of porous substance with subcritical density, Matter Radiat. Extremes **9**, 016601 (2024).

[46] O. N. Rosmej, M. Gyrdymov, N. E. Andreev, P. Tavana, V. Popov, N. G. Borisenko, A. I. Gromov, S. Y. Gus'kov, R. Yakhin, G. A. Vegunova, N. Bukharskii, P. Korneev, J. Cikhardt, S. Zähter, S. Busch, J. Jacoby, V. G. Pimenov, C. Spielmann, and A. Pukhov, Advanced plasma target from pre-ionized low-density foam for effective and robust direct laser acceleration of electrons, High Power Laser Sci. Eng. **13**, e3 (2025).

[47] T. Bonnet, M. Comet, D. Denis-Petit, F. Gobet, F. Hannachi, M. Tarisien, M. Versteegen, and M. M. Aléonard, Response functions of imaging plates to photons, electrons and ^{4}He particles, Rev. Sci. Instrum. **84**, 103510 (2013).

[48] M. M. Günther, A. Britz, R. J. Clarke, K. Harres, G. Hoffmeister, F. Nürnberg, A. Otten, A. Pelka, M. Roth, and K. Vogt, NAIS: Nuclear activation-based imaging spectroscopy, Rev. Sci. Instrum. **84**, 073305 (2013).

[49] W. Schumaker, G. Sarri, M. Vargas, Z. Zhao, K. Behm, V. Chvykov, B. Dromey, B. Hou, A. Maksimchuk, J. Nees, V. Yanovsky, M. Zepf, A. G. R. Thomas, and K. Krushelnick, Measurements of high-energy radiation generation from laser-wakefield accelerated electron beams, Phys. Plasmas **21**, 056704 (2014).

[50] Y.-R. Shou, X.-Z. Wu, G.-E. Ahn, S. Y. Kim, S. H. Kim, H. W. Lee, J. W. Yoon, J. H. Sung, S. K. Lee, X.-Q. Yan, I. W. Choi, and C. H. Nam, Spatial and spectral measurement of laser-driven protons through radioactivation, Nucl. Sci. Tech. **34**, 183 (2023).

[51] H Ing, R. A. Noulty, and T. D. McLean, Bubble detectors—a maturing technology, Radiat. Meas. **27**, 1 (1997).

[52] A. Mangiarotti and M. N. Martins, A review of electron–nucleus bremsstrahlung cross sections between 1 and 10 MeV, Radiat. Phys. Chem. **141**, 312 (2017).

[53] S. Agostinelli *et al.*, Geant4—a simulation toolkit, Nucl. Instrum. Methods Phys. Res., Sect. A **506**, 250 (2003).

[54] S. M. Seltzer and M. J. Berger, Bremsstrahlung energy spectra from electrons with kinetic energy 1 KeV–10 GeV incident on screened nuclei and orbital electrons of neutral atoms with $z = 1$–100, At. Data Nucl. Data Tables **35**, 345 (1986).

[55] M. M. Günther, K. Sonnabend, E. Brambrink, K. Vogt, V. Bagnoud, K. Harres, and M. Roth, A novel nuclear pyrometry for the characterization of high-energy bremsstrahlung and electrons produced in relativistic laser-plasma interactions, Phys. Plasmas **18**, 083102 (2011).

[56] A. J. Koning, in *AIP Conference Proceedings* (AIP, 2005), pp. 1154–1159.

[57] N. Otuka *et al.*, Towards a more complete and accurate experimental nuclear reaction data library (EXFOR): International collaboration between nuclear reaction data centres (NRDC), Nucl. Data Sheets **120**, 272 (2014).

[58] IEEE, American National Standard for Calibration and Use of Germanium Spectrometers for the Measurement of Gamma-Ray Emission Rates of Radionuclides (1999), pp. 1–76, https://doi.org/10.1109/IEEESTD.1999.89430.

[59] G. Boutoux, N. Rabhi, D. Batani, A. Binet, J.-E. Ducret, K. Jakubowska, J.-P. Nègre, C. Reverdin, and I. Thfoin, Study of imaging plate detector sensitivity to 5–18 MeV electrons, Rev. Sci. Instrum. **86**, 113304 (2015).

[60] Guide for physics lists—physicslistguide 11.3 documentation (12/9/2024). https://geant4-userdoc.web.cern.ch/UsersGuides/PhysicsListGuide/html/index.html.

[61] Martin J. Berger and Stephen M. Seltzer, *Tables of energy losses and ranges of electrons and positrons* (1964), https://ntrs.nasa.gov/api/citations/19650002905/downloads/19650002905.pdf.

[62] N. Lemos *et al.*, X-ray sources using a picosecond laser driven plasma accelerator, Phys. Plasmas **26**, 083110 (2019).

[63] C. Courtois, R. Edwards, A. La Compant Fontaine, C. Aedy, S. Bazzoli, J. L. Bourgade, J. Gazave, J. M. Lagrange, O. Landoas, L. Le Dain, D. Mastrosimone, N. Pichoff, G. Pien, and C. Stoeckl, Characterisation of a MeV

bremsstrahlung x-ray source produced from a high intensity laser for high areal density object radiography, Phys. Plasmas **20**, 083114 (2013).

[64] H. Chen *et al.*, Progress towards a laser produced relativistic electron-positron pair plasma, J. Phys. Conf. Ser. **688**, 012010 (2016).

[65] Tavana, Ultra-high Flux of Direct Laser Accelerated Electrons, MeV Photons and Neutrons using Overdense Foams, Zenodo (2025), https://doi.org/10.5281/zenodo.17939742.

[66] M. Rising *et al.*, Mcnp® code v.6.3.0 release notes, https://doi.org/10.2172/1909545.